GLC_FCS30D: The first global 30-m land-cover dynamic monitoring product with a fine classification system from 1985 to 2022 using dense time-series Landsat imagery and continuous change-detection method

Xiao Zhang[1, 2], Tingting Zhang[1, 4], Hong Xu[5], Wendi Liu[1, 2, 3], Jinqing Wang[1, 2, 3], Xidong Chen[6], Liangyun Liu[1, 2, 3, *]

1 International Research Center of Big Data for Sustainable Development Goals, Beijing 100094, China

2 Key Laboratory of Digital Earth Science, Aerospace Information Research Institute, Chinese Academy of Sciences, Beijing 100094, China

3 School of Electronic, Electrical and Communication Engineering, University of Chinese Academy of Sciences, Beijing 100049, China

4 College of Geomatics, Xi'an University of Science and Technology, Xi'an 710054, China

5 The High-Tech Research & Development Center (HTRDC) of the Ministry of Science & Technology, Beijing 100044, China

6 Future Urbanity & Sustainable Environment (FUSE) Lab, The University of Hong Kong, Hong Kong, 999007, China

* Corresponding author Email: liuly@radi.ac.cn

Abstract

Land cover change has been identified as an important cause or driving force of global climate change and is a significant research topic. Over the past few decades, global land-cover mapping has progressed, however, long time-series global land-cover change monitoring data are still sparse, especially at 30-m resolution. In this study, GLC_FCS30D is described as the first global 30-m land-cover dynamic monitoring dataset, containing 35 land-cover subcategories and covering the period of 1985–2022 with 26 time-steps (maps updated every five years before 2000 and annually after 2000). GLC_FCS30D has been developed using continuous change detection and all available Landsat imagery based on the Google Earth Engine platform. In specific, we first take advantage of the continuous change-detection model and full time-series Landsat observations to capture the time-points of changed pixels and identify the temporally stable areas. Then, we apply a spatiotemporal refinement method to derive the globally distributed and high-confidence training samples from these temporally stable areas. Next, locally adaptive classification models are used to update the land-cover information for the changed pixels, and a temporal-consistency optimization algorithm is adopted to improve their temporal stability and suppress some false changes. Further, the GLC_FCS30D product is validated using 84,526 globally distributed validation samples in 2020 and achieves an overall accuracy of 80.88% ($\pm$0.27%) for the basic classification system (10 major land-cover types) and 73.24% ($\pm$0.30%) for the LCCS level-1 validation system (17 LCCS land-cover types). Meanwhile, two third-party time-series validation datasets in the United States and Europe Union are also collected for analyzing accuracy variations, and the results show that the GLC_FCS30D offers significant stability for time-series accuracy variation and achieves the mean accuracies of 79.50% ($\pm$0.50%) and 81.91% ($\pm$0.09%) over the two regions. Last, we conclude the global land-cover change information from GLC_FCS30D dataset, namely, the forest and cropland variations dominate global land cover change over past 37 years, and net loss of forests reaches about 2.5 million km^2 and net gain in cropland area is approximately 1.3 million km^2. Therefore, the novel GLC_FCS30D is an accurate time-series land-cover dynamic monitoring product benefiting from its diverse classification system, high spatial resolution

and the long time span of 1985–2022, thus, it will effectively support global climate change research and promote sustainable development analysis. The GLC_FCS30D datasets are available via https://doi.org/10.5281/zenodo.8239305 (Liu et al, 2023).

Keywords: GLC_FCS30D, 1985-2022, Land-cover change, Landsat, change detection, Google Earth Engine

45 1. Introduction

Land cover data are important and necessary for supporting sustainable development goals, maintaining biodiversity, and monitoring natural resources (Liu et al., 2021b; Potapov et al., 2022). The land cover changes directly or indirectly influence the global climate patterns and the speed and magnitude of climate change (Song et al., 2018) and increasingly affects biogeochemical cycles, the carbon cycle, and Earth's energy balance (Foley
50 et al., 2005; Hong et al., 2021; Winkler et al., 2021). Since the industrial revolution, under the dual pressure of global climate change and human activities, global land cover has undergone drastic changes. According to a Global Carbon Project report in 2020, since the industrialization period, land cover and land use changes have contributed to approximately 25% of global greenhouse gas emissions (Friedlingstein et al., 2020), and this trend is exacerbated with the ongoing increase in population and per capita energy consumption (Xian et al.,
55 2022). Therefore, understanding and studying land cover changes are of vital significance for addressing global environmental changes, promoting sustainable development, and safeguarding the Earth's ecological environment.

Remote-sensing techniques, with periodic Earth observation capability and archived massive long-term observation data since 1972, provide the most cost-effective and practical solutions for long time-series large-
60 area land-cover change monitoring. In the past few decades, with the continuous improvement of remote sensing technology and storage and computing capabilities, global land-cover change monitoring (GLCCM) has transitioned from 1-km spatial resolution to fine resolution of 30-m or 10-m and from single-phase mapping to long-term monitoring (Ban et al., 2015; Friedl et al., 2010; Friedl et al., 2022; Giri et al., 2013). In the early stage, GLCCM mainly relied on the time-series MODIS, AVHRR, and Project for Onboard Autonomy
65 (PROBA)-V imagery; for example, Sulla-Menashe et al. (2019) generated a global 500-m annual land-cover products (MCD12Q1) from 2001 to present using time-series MODIS imagery with an overall accuracy of 73.6%. Defourny et al. (2018) integrated time-series PROBA-V and Medium Resolution Imaging Spectrometer (MERIS) observations to develop a global 300-m annual land-cover dynamic dataset (CCI_LC) from 1992 to 2020 with an overall accuracy of 71.5%. These coarse land-cover change products comprehensively captured
70 the spatial patterns of various land-cover types and quantified the global land-cover changes caused by human and natural activities. However, they still had major limitations especially in regions with intense human activity and high spatial heterogeneity because these broken and heterogeneous land-cover changes cannot be captured by coarse-resolution satellite observations (Hansen et al., 2013; Herold et al., 2008; Liu et al., 2021b; Zhang et al., 2021c).

75 Recently, benefitting from the free access to fine-resolution satellite imagery and powerful computing and storage capabilities, especially after the rise of cloud computing [such as Google Earth Engine (Gorelick et al., 2017) and Microsoft Planetary Computer], fine-resolution land-cover dynamic monitoring is experiencing rapid development. Correspondingly, numerous national and global 30-m land-cover dynamic products have been developed (Homer et al., 2020; Liu et al., 2021a; Potapov et al., 2022; Yang and Huang, 2021; Zhang et al.,
80 2022). For example, Yang and Huang (2021) used China's land-use/cover datasets (CLUDs) as the prior dataset

and then combined multitemporal classification and spatiotemporal consistency post-processing method to develop an annual 30-m land cover dataset (CLCD) for China from 1990 to 2019. Similarly, Liu et al. (2021a) combined pixel-based classification and spatiotemporal post-processing method to generate the first global 30-m land-cover change products. However, many studies have demonstrated that multiperiod independent classifications lead to significant classification error accumulation in time-series land-cover change monitoring (Sulla-Menashe et al., 2019; Zhu, 2017). For example, Xian et al. (2022) stated that the independent classification strategy suffered the constraints of post-processing requirements, for ensuring the temporal consistency of land-cover change maps. Therefore, although GLCCM has progressed significantly over the past few decades, an accurate global 30-m land-cover change-detection product generated by an efficient land-cover change method is still urgently required.

One of the greatest challenges for large-area land-cover change detection is to select the optimal algorithm to capture the land-cover changes from time-series observations (Healey et al., 2018; Zhu, 2017). Over past few decades, a series of change-detection algorithms have been proposed for monitoring forest disturbance (Huang et al., 2009; Jin et al., 2023; Kennedy et al., 2007; Kennedy et al., 2010; Qin et al., 2021), urban expansion (Liu et al., 2019; Zhang et al., 2021a), cropland dynamics (Dong et al., 2015; Potapov et al., 2021), and land-cover changes (Bullock et al., 2019; Jin et al., 2017; Verbesselt et al., 2010; Zhu et al., 2019). However, most of them were only suitable for regional land-cover change monitoring and some of the algorithms needed prior knowledge (such as for urban expansion). Zhu (2017) systematically reviewed the performances and limitations of various change-detection methods based on multitemporal satellite data, and further explained that the high temporal frequency and multivariate change-detection algorithms are more suitable for large-area and long time-series land-cover changes after solving a problem with a huge amount of computation. Similarly, Xian et al. (2022) and Liu et al. (2019) concluded that dense and continuous change-detection methods had higher accuracy and more robustness than traditional change-detection methods for capturing multiple, complicated changes.

Continuous Change Detection and Classification (CCDC) algorithm, a classical change-detection method based on dense time-series observations proposed by (Zhu and Woodcock, 2014b), is widely used for regional and national land-cover monitoring (Xian et al., 2022; Xie et al., 2022). It used all available Landsat observations to build time-series regression models and then captured the outliers by analyzing the differences between the actual observations and model estimations. Zhu and Woodcock (2014b) demonstrated that the CCDC algorithm attained a general accuracy of 90% and temporal accuracy of 80% for capturing land-cover changes. Thus, it has been adopted by the United States Geological Survey (USGS) as the official algorithm for monitoring land-cover changes over the United States (Pengra et al., 2016). For example, Xian et al. (2022) implemented the CCDC algorithm and all available Landsat data to develop annual land-cover change products over the contiguous United States (CONUS) for 1985–2017 with an overall accuracy of 82.5%.

In summary, over the past decades, land-cover mapping and monitoring has made significant progress; however, time-series global 30-m land-cover dynamic products derived from change-detection algorithms are still lacking. In this study, we had the following three aims: 1) use the continuous change-detection algorithm and full time-series Landsat observations to generate the first global 30-m land-cover dynamic products with fine classification system (GLC_FCS30D) from 1985 to 2022, which contains 35 fine land-cover subcategories with 26 time-steps (maps updating every five years before 2000 and annually after 2000); 2) quantify the land-cover changes and analyze the spatiotemporal change patterns of various land-cover types based on the

developed GLC_FCS30D dataset; and 3) quantitatively analyze the performance of the GLC_FCS30D product using multisourced validation datasets.

2. Datasets

2.1 Continuous Landsat imagery from 1984 to 2022

125   All available Landsat imagery from 1984 to 2022, covering Landsat 5 Thematic Mapper (TM), Landsat 7 Enhanced Thematic Mapper Plus (ETM+), Landsat 8 Operational Land Imager (OLI), and Landsat 9 OLI missions, was collected via the GEE cloud-computing platform. Specific measures were taken to build a high-quality continuous time-series Landsat collection. First, all Landsat images underwent atmospheric correction to convert them to surface reflectance using the Landsat Ecosystem Disturbance Adaptive Processing System

130   (LEDAPS) and Land Surface Reflectance Code (LaSRC) methods (Vermote, 2007; Vermote and Kotchenova, 2008). Then, the CFmask algorithm, which and has high accuracy and good robustness in cloud and shadow detection and is also the official cloud- and shadow detection algorithm of the USGS, was applied to mask poor-quality observations, including cloud, shadow, and saturated pixels. (Zhu et al., 2015; Zhu and Woodcock, 2014a). Last, although the Landsat 5, 7, 8, and 9 missions share similar spectral bands, the wavelength

135   differences between the ETM+ and OLI cannot be ignored. Relative radiometric normalization was applied to the TM and ETM+ imagery using the transformation coefficients suggest by Roy et al. (2016).

2.2 Global land-cover dataset at 30 m for the year of 2020

    The global 30-m land-cover product with fine classification system in 2020 (GLC_FCS30-2020), is the baseline for generating training samples and identifying land-cover information in the temporally stable regions

140   in Section 3. The GLC_FCS30 dataset was developed using locally adaptive classifications and confident and globally distributed training samples in their developed global spatiotemporal spectra library, and then validated to reach an overall accuracy of 82.5% with the basic validation system (Zhang et al., 2021b). Cross-comparisons with other land-cover products showed obvious advantages for the GLC_FCS30 in mapping accuracy and diversity of land-cover types. The GLC_FCS30-2020 dataset is freely available at

145   https://doi.org/10.5281/zenodo.4280923 (Liu et al., 2020).

2.3 Global impervious surface dynamic dataset at 30 m from 1985 to 2022

    Many studies found that high spatiotemporal heterogeneity and broken constructs of impervious surface caused high uncertainty and difficulty in monitoring their dynamics (Gong et al., 2019; Zhang et al., 2022), and change detection methods also face issues of both missed detections and false alarms when applied to the

150   dynamic monitoring of heterogeneous impervious surfaces. Thus, we independently produced a time-series global impervious surface dynamic dataset at 30 m (GISD30) during 1985–2022 and then overlaid this thematic dataset on the GLC_FCS30D dataset to ensure their high confidence in the impervious surface dynamics. The GISD30 dataset was developed by combining the sample migration, spectra generalization and local adaptive modeling methods, and then optimized by the spatiotemporal-consistency correction method (Zhang et al.,

155   2022). It was validated to attain the mean accuracy of 90.1% over the globe and to perform better than other similar products in capturing the changes in impervious surfaces over time and across different types of landscapes. At the same time, third-party validation also indicated that GISD30 exhibited superior performance among similar global 30-meter impervious surface products (Wang et al., 2022).

2.4 Global 30-m wetland datasets from 1985 to 2022

160   Like the impervious surface, the global wetland dynamic dataset is independently produced because the reflectance spectra of the wetland and phenological variations changed daily with the water levels. The continuous change-detection method would suffer serious commission and omission errors for wetland dynamic monitoring (Gallant, 2015). In this study, the GWL_FCS30 (global 30-m wetland map with a fine classification system) wetland dataset from 1985 to 2022, developed by integrating the automatic sample extraction method,

165   a stratified classification strategy, and time-series Landsat observations (Zhang et al., 2023), would be superimposed on the GLC_FCS30D land-cover dynamic dataset. The GWL_FCS30 was quantitatively assessed to the mean accuracy of 86.44% using 25708 validation points, and demonstrated the highest level of performance among other wetland products when it came to capturing the spatial patterns of wetlands during cross-comparisons (Zhang et al., 2023). GWL_FCS30 further splits the wetland into seven wetland

170   subcategories (four inland and three coastal subcategories), and would be overlaid directly onto the GLC_FCS30D dataset not only improves the monitoring accuracy of wetland but also riches the number of land cover types (in Table 1).

2.5 Validation datasets

   To comprehensively analyze the accuracy metrics for the GLC_FCS30D dataset, two types of validation

175   datasets were collected, including: an independent global validation dataset from 2020 and two third-party time-series validation datasets for the United States and the European Union.

2.5.1 Global validation dataset

   A total of 84,526 globally distributed validation samples are collected to analyze the accuracy metrics for the GLC_FCS30D dataset in 2020, and their spatial distributions are illustrated in Figure 1. Intuitively, the

180   spatial patterns of the global validation dataset are consistent with the actual global land-cover situation. Specifically, to ensure the confidence and rationality of the validation datasets, several measures are taken, which were explained in detail in our previous work (Zhao et al. (2023). First, a stratified random sampling method is applied by combining the landscape heterogeneity, population density data and Köppen climate groups, which effectively increases the sample size in the heterogeneous landscapes and for these rare land-

185   cover types. Second, for each validation sample, the land-cover type is determined through independent interpretation by trained interpreters after combining high-resolution aerial photography, multitemporal Landsat images, and other relevant ancillary datasets (such as: vegetation coverage, tree height, phenological curves, , and terrain characteristics). Independent interpretation software has also been developed based on the GEE platform (https://eliza-ting.users.earthengine.app/view/crd-vit) for efficiently recognizing the land cover types

190   of each sample. Third, a quality-controlled operation, based on duplicate interpretations, is further used to ensure the confidence level of each validation sample. Each sample is independently labeled by three junior interpreters and then double-checked by the senior experts, and validation samples with huge disparities would be discarded. In addition, because the impervious surface and wetland datasets have been independently produced and validated in our previous works (Zhang et al., 2023; Zhang et al., 2022), the corresponding high-quality

195   validation samples of these two thematic types are also imported to the global validation datasets.
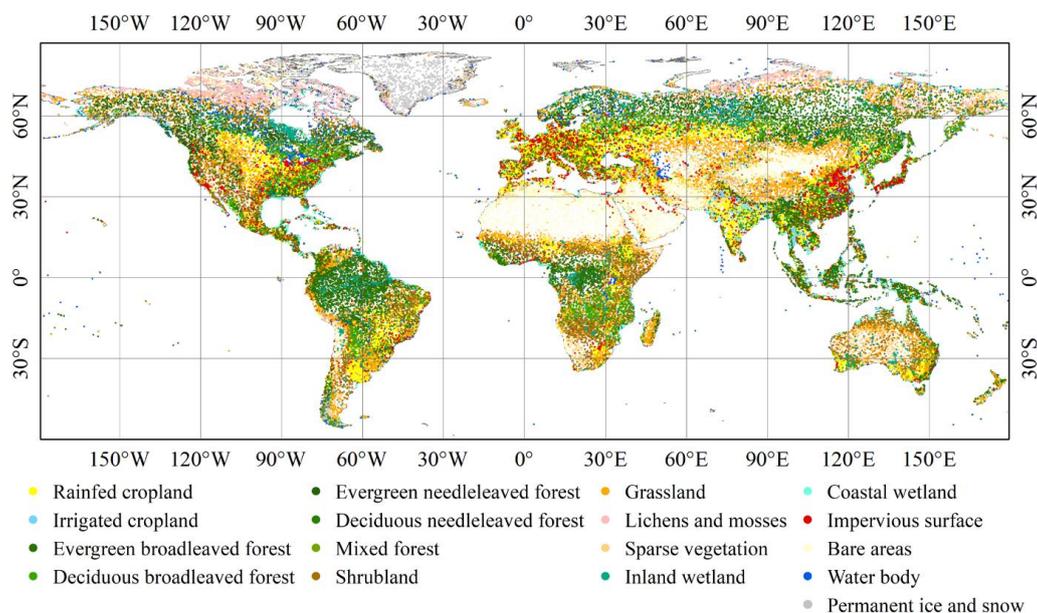
Figure 1. Spatial distribution of 84,526 global validation points containing 17 fine land-cover types in the normal year of 2020.

2.5.2 Third-party regional time-series validation datasets

200   Due to the great difficulty in the collection of long time-series global validation datasets, we used two third-party regional datasets for the CONUS and the European Union. The first time-series validation dataset was assessed the performance of the Land Cover Monitoring, Assessment, and Projection (LCMAP) Collection 1.0 annual land cover products (Stehman et al., 2021) (called LCMAP_Val, https://www.usgs.gov/special-topics/lcmap/validation-data). The LCMAP_Val consisted of 24,971 validation samples with 30-m spatial

205   resolution and covered time period of 1985 to 2017. It developed by combining a simple random sampling method and visual interpretation from high-resolution aerial photography, multitemporal Landsat images, as well as other auxiliary datasets. Meanwhile, to guarantee the reliability of each validation sample, the TimeSync auxiliary tool was also adopted to capture the land-cover changes (Stehman et al., 2021). Quality control was implemented through duplicate interpretations (Xian et al., 2022).

210   The second regional validation dataset was the Land Use/Cover Area frame Survey (LUCAS), which is the most comprehensive and largest land-cover validation dataset in the European Union and is freely available at https://land.copernicus.eu/imagery-in-situ/lucas. It contains 1,090,863 validation points based on a systematic 2 km × 2 km grid and covers the period of 2006 to 2018 with an interval of 3 years (d'Andrimont et al., 2020). Five LUCAS surveys in 2006, 2009, 2012, 2015, and 2018 assessed the time-series accuracies of the

215   GLC_FCS30D. The LUCAS is developed from a combination of field observations and photo interpretation (Büttner and Eiselt, 2013; Ballin et al., 2018); thus, it performs with high confidence and also attracts widespread attention in land-cover validations (Gao et al., 2020; Venter et al., 2022).

3. Methods

Figure 2 presents a detailed flowchart for monitoring land-cover changes by combining the Continuous Change Detection (CCD) algorithm, proposed by Zhu and Woodcock (2014b), and the local adaptive updating method. Specifically, the flowchart contains four main procedures including: (1) detecting the temporally stable pixels and the time-points of abrupt changes in these changed land-cover pixels from the continuous change-detection model; (2) deriving the spatiotemporally stable training samples by using the spatiotemporal refinement method from GLC_FCS30 land-cover products and temporally stable masks; (3) building the local adaptive classification models for each local region and then updating the land-cover information in the changed pixels; and (4) using the spatiotemporal consistency optimization method to improve the quality of land-cover change maps and suppress these false changes.
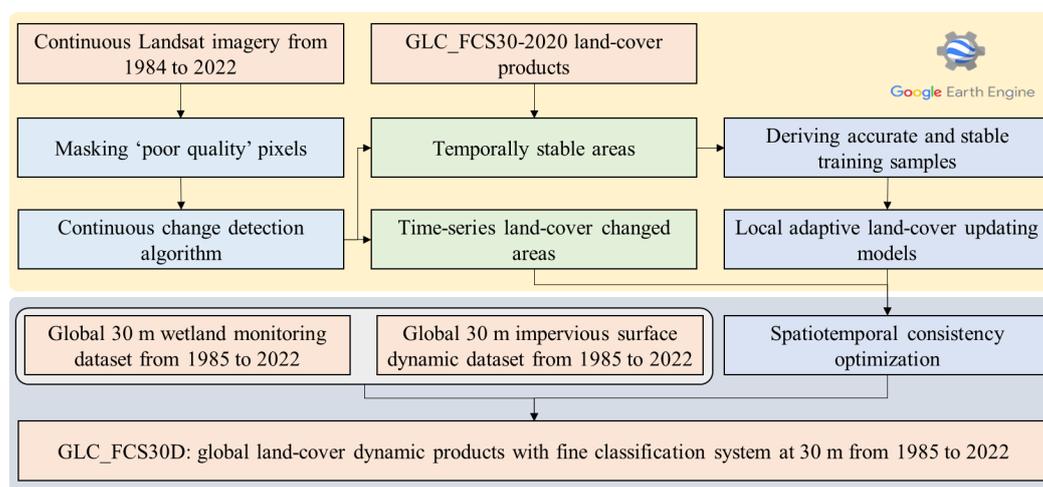
Figure 2. The flowchart of the proposed method combining the continuous change-detection (CCD) algorithm and a local adaptive updating algorithm.

3.1 The fine classification system used in the GLC_FCS30D

Determining the classification system is usually a prerequisite for land-cover mapping and monitoring. In this study, as we used the GLC_FCS30-2020 as the baseline land-cover product, and further overlaid the GWL_FCS30 dataset on the GLC_FCS30D to ensure high accuracy in the wetland areas; thus, the fine classification system used in this study would inherit from that of the GLC_FCS30-2020 and GWL_FCS30. Table 1 lists the details of the fine classification system. It contains 35 fine land-cover types and has obvious advantages over identifying the forest and wetland subcategories.

Table 1. The details of the fine classification system in the GLC_FCS30D land-cover dynamic dataset.

Basic classification system	Level-1 validation system	Fine classification system	Id
Cropland	Rainfed cropland	Rainfed cropland	10
		Herbaceous cover cropland	11
		Tree or shrub cover cropland	12
	Irrigated cropland	Irrigated cropland	20
Forest	Evergreen broadleaved forest	Closed evergreen broadleaved forest	51
		Open evergreen broadleaved forest	52

		Closed deciduous broadleaved forest	61
	Deciduous broadleaved forest	Open deciduous broadleaved forest	62
	Evergreen needleleaved forest	Closed evergreen needleleaved forest	71
		Open evergreen needleleaved forest	72
	Deciduous needleleaved forest	Closed deciduous needleleaved forest	81
		Open deciduous needleleaved forest	82
	Mixed-leaf forest	Closed mixed-leaf forest	91
		Open mixed-leaf forest	92
Shrubland	Shrubland	Shrubland	120
		Evergreen shrubland	121
		Deciduous shrubland	122
Grassland	Grassland	Grassland	130
Tundra	Lichens and mosses	Lichens and mosses	140
Wetland	Inland wetland	Swamp	181
		Marsh	182
		Flooded flat	183
		Saline	184
	Coastal wetland	Mangrove	185
		Salt marsh	186
		Tidal flat	187
Impervious surface	Impervious surface	Impervious surface	190
Bare areas	Sparse vegetation	Sparse vegetation	150
		Sparse shrubland	152
		Sparse herbaceous cover	153
	Bare areas	Bare areas	200
		Consolidated bare areas	201
		Unconsolidated bare areas	202
Water body	Water body	Water body	210
Permanent snow and ice	Permanent snow and ice	Permanent snow and ice	220

3.2 Detecting changes using the CCD algorithm and continuous Landsat imagery

240   In general, land-cover changes can be grouped into three categories including: periodic changes caused by the phenological variability, trend changes driven by natural behavior (such as vegetation growth), and abrupt changes caused by natural or human disturbances (such as deforestation, urban expansion). Thus, capturing these abrupt changes and simultaneously suppressing the periodic and trend changes are the key to land-cover monitoring. In this study, the CCD algorithm (Zhu and Woodcock (2014b) captured these abrupt changes. The
245   algorithm uses Fourier transformation to fit the time-series observations with the trend term (estimating the trend changes) and harmonic terms (describing the periodic changes) in Eq. (1).

$$\hat{\rho}(i,t) = a_{0,i} + c_{1,i} \times t + \sum_{k=1}^{n}\left(a_{k,i} \times cos\left(\frac{2k\pi}{T}t\right) + b_{k,i} \times sin\left(\frac{2k\pi}{T}t\right)\right) \tag{1}$$

where $\hat{\rho}(i,t)$ represents the predicted value of the ith band at the tth Julian day, $c_{1,i}$ and $a_{0,i}$ are the regression slope and intercept of the ith band, $a_{k,i}$ and $b_{k,i}$ represent the coefficients of the kth order

harmonic term for the ith band, n denotes the number of harmonic terms, and T is the day number of the
year (usually defined as 365). As for how to determine value of n, Zhu and Woodcock (2014b) explained that
higher order harmonic terms have better performance for capturing the periodic variability, but caused
overfitting in the time-series model and needed more clear-sky observations to initialize the coefficients of $a_{k,i}$
and $b_{k,i}$. After balancing the advantages and disadvantages of the higher order harmonic terms, we finally chose
n as 3, as suggested by other studies (Xian et al., 2022; Xie et al., 2022).

Then, as the CCD is a multivariate change-detection algorithm for capturing the changes of various land-
cover types Zhu (2017), five Landsat spectral bands (excluding the blue band for minimizing the effects of the
atmosphere and clouds), and three spectral indexes [including: NDVI, NDWI, and NBR as given in Eq. (2)]
were combined to detect many kind of changes in the Landsat time-series.

$$NDVI = \frac{\rho_{nir} - \rho_r}{\rho_{nir} + \rho_r}, \quad NDWI = \frac{\rho_{green} - \rho_{swir1}}{\rho_{green} + \rho_{swir1}}, \quad NBR = \frac{\rho_{nir} - \rho_{swir1}}{\rho_{nir} + \rho_{swir1}} \tag{2}$$

where ρ_{green}, ρ_r, ρ_{nir} and ρ_{swir1} are the green, red, NIR, SWIR1 and SWIR2 spectral bands in the Landsat
imagery. Next, to determine the fitted coefficients of the kth order harmonic term in Eq. (1), the Least Absolute
Shrinkage and Selection Operator (LASSO) regression algorithm was applied, which demonstrated better
performance than the traditional Ordinary Least Squares method in reducing the overfitting problem and dealing
with unevenly distributed and sparse Landsat observations (Zhu and Woodcock (2014b).

After modeling the time-series observations using the CCD algorithm, we can analyze the land-cover
changes from the differences between actual observations and predicted values in the time-series fitting models.
Figure 3 shows three typical scenarios in which land-cover dynamics were modeled by the CCD algorithm.
Specifically, Figure 3a illustrates that there was no abrupt break in the whole period and thus only the single
time-series model was built, and the pixel was usually labeled as temporally stable. Figure 3b indicates that the
pixel underwent an abrupt change and the time-series observations were split into two segments. The time point
of the abrupt change occurred around 1996. Figure 3c gives a complicated time-series disturbance example, in
which multiple abrupt changes were detected and the time-series observations were split into four segments.
The time-series models for segments 1, 2, and 4 showed obvious trend changes.
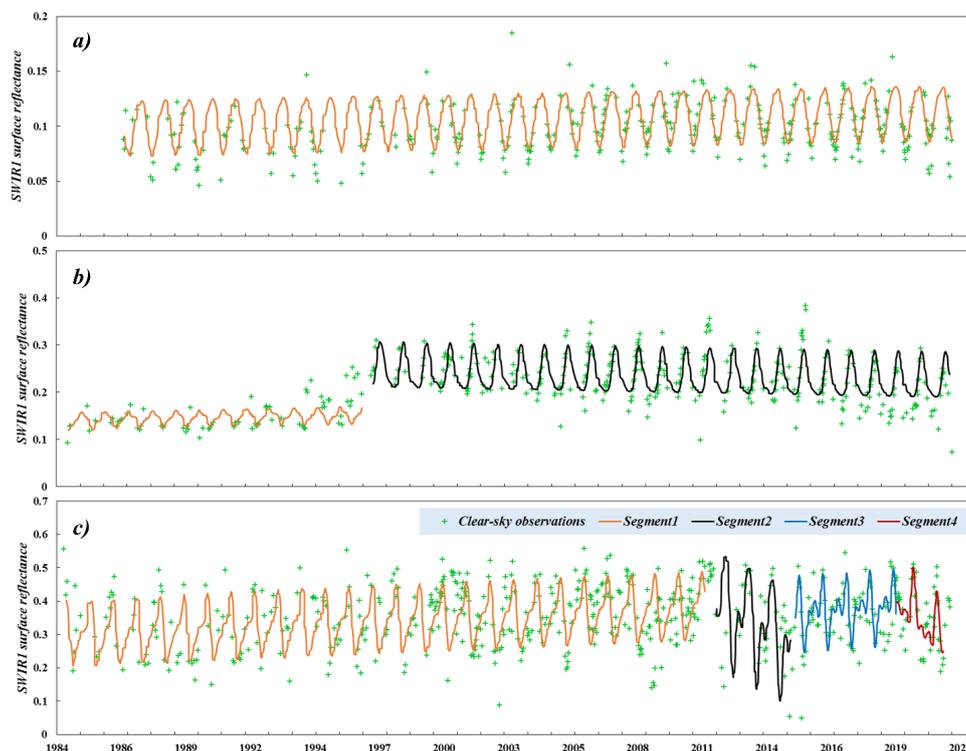
Figure 3. Three typical land-cover changes using the continuous change detection (CCD) algorithm and
275   continuous Landsat observations; a) time-series stable land-cover condition; b) one single abrupt change; c)
multiple abrupt changes.

3.3 Updating changed areas using local adaptive classifications

Using the CCD algorithm and continuous Landsat imagery, we identified the temporally stable pixels and
the time points of abrupt changes for the land-cover change pixels. Accurately determining land-cover labels of
280   the changed pixels (or understanding the change process 'from-to') is another key procedure for time-series
land-cover monitoring. To achieve this goal, we derived spatiotemporally stable training samples (see Section
3.3.1), then updated the changed pixels using multitemporal classifications, and finally minimized the
cumulative error caused by independent classifications.

3.3.1 Deriving spatiotemporally stable training samples

285   Numerous studies demonstrated that the accurateness of the training samples plays a critical role in accurate
mapping (Foody and Arora, 2010; Zhang et al., 2020). Visual interpretation can ensure high-confidence samples
at the expense of a large quantity of manual participations, so it was not suitable for collecting large-area training
samples. An alternative option involved generating training samples by refining existing land-cover products
through a series of improvement measures (Zhang et al., 2021b; Zhang et al., 2023). Inspired by the latter option,
290   we combined the GLC_FCS30-2020 prior dataset and a change-detection mask (derived from the CCD
algorithm described in Section 3.2) to obtain the spatiotemporally stable training samples. Specifically,
temporally stable areas are known to have higher mapping accuracy (Yang and Huang, 2021; Zhang and Roy,

2017; Zhang et al., 2023); thus, we first used the CCD mask to retain these temporally stable areas in the GLC_FCS30-2020 maps. Radoux et al. (2014) emphasized that land-cover transition areas usually were subject
295   to more serious misclassification problems and that the homogeneous land-cover pixels had a higher probability of achieving acceptable accuracy. Therefore, we used the morphological erosion filter of 3 pixels × 3 pixels to refine the GLC_FCS30-2020 maps into spatially homogeneous areas. After identifying the intersection of temporally stable and spatially homogenous areas, we retained these as the spatiotemporally stable training sample candidates.

300   Numerous studies have highlighted the importance of training sample balance and distribution, as they significantly influence the mapping performance (Foody, 2009; Jin et al., 2014; Millard and Richardson, 2015). First, in term of the sample distribution, there are two options for training sample distribution including areal-proportional or equal allocation, and former was demonstrate to achieve higher accuracy than the latter option in land-cover mapping especially in complicated land-cover conditions (Jin et al., 2014). However, when using
305   the areal-proportional sampling strategy, the rare land-cover types usually had small sample sizes and would be sacrificed because the aim of land-cover mapping was to achieve a global optimum rather than a local optimum. Thus, the maximum and minimum sample size for abundant and rare land-cover types were suggested as 8000 and 600, came from the study in Zhu et al. (2016), for avoiding the extremes of sample sizes. Next, the GLC_FCS30-2020 products were split into 961 5° × 5° geographical tiles, and we used the areal-proportional
310   sampling strategy and sample balancing parameters to allocate the training samples from the spatiotemporally stable areas in each 5° × 5° geographical tile. Last, the impervious surface and wetland samples were excluded because both have been independently developed as the thematic datasets in Section 2.3 and 2.4.

3.3.2 Updating changed areas using local adaptive classifications

Before building the local adaptive classification models, we must extract useful spectral features from the
315   time-series Landsat observations. In this study, we used multitemporal phenological, texture, and topographical features. Specifically, the multitemporal phenological features were extracted by using the percentile-compositing method, which has fewer constraints than other compositing algorithms (such as the seasonal-based compositing method) while achieving similar mapping accuracy (Azzari and Lobell, 2017). The time-series Landsat spectral bands (five optical bands after excluding atmospherically sensitive blue band) and
320   corresponding spectral indexes [NDVI, NDWI, and NBR in Eq. (2)] were composited into five percentiles (10th, 25th, 50th, 75th, and 90th). Next, in terms of the texture features, our previous study explained that the texture features had positive contribution on land-cover mapping (Zhang et al. (2021b), so the gray-level co-occurrence matrix method was used for the 50th-percentile–composited NIR band to extract the homogeneity, entropy, dissimilarity, variance, contrast, and correlation. Last, since the land-cover distribution was usually related to
325   the topographical environment, for example, croplands and water bodies are mainly distributed in flat areas, three topographical variables (elevation, slope, and aspect), calculated from a global 30 m DEM dataset (named as: ASTER_GDEM) (Tachikawa et al., 2011), were also imported. In total, there were 49 multisource features, including 40 phenological spectra features, 6 texture features, and 3 topographical variables.

There are two options for global land-cover mapping and updating: global modeling and local adaptive
330   modeling, and our previous studies have explained that local adaptive modeling yields superior results compared to global modeling. This is primarily due to the former's capability to take regional characteristics into account more effectively, leading to increased sensitivity in training samples and higher accuracy in land-cover classification (Zhang et al., 2021b; Zhang et al., 2023; Zhang et al., 2022). Thus, we first inherited the regional

gridding style in the GLC_FCS30 (Zhang et al., 2021b), namely, the global land was divided into 961 5° × 5°
geographical tiles. Afterward, the local classification models were independently built for updating the land
cover in each tile using the corresponding training samples in the neighboring eight surrounding tiles at 3 × 3
window. The adjacent training samples were imported to increase the continuity of the adjacent land-cover maps.

Last, in the selection of the suitable classification algorithm, random forest (RF) classifier has significant
advantages, including: accommodating high-dimensional training features, better ability to deal with the
overfitting problem, and higher classification accuracy than other widely used classifiers (Belgiu and Drăguţ,
2016; Gislason et al., 2006). Meanwhile, the RF algorithm was also integrated into the internal function library
of the GEE cloud platform as *ee.Classifier.smileRandomForest()*. Thus, the RF algorithm was used to combine
the training samples and multisourced features for updating the changed pixels. The RF algorithm allows for
adjusting two key parameters, for which the default recommended values were used based on previous studies
(Belgiu and Drăguţ, 2016; Zhang et al., 2019).

3.3.3 Temporal-consistency optimization

To ensure the rationality and consistency of land-cover changes for long time-series, the CCD algorithm
was applied to capture the time points of land-cover changes, and then the changed pixels were updated using
the local adaptive classifications. In this study, despite our best efforts, it was difficult to completely eliminate
classification errors, particularly when dealing with changes over time. To address this issue and enhance
accuracy in areas with temporal variations, we employed the temporal consistency optimization method
described in Eq. (3). This approach incorporates both temporal and spatial neighboring information to assess
homogeneity, thereby reducing potential misclassifications in time-series changed areas.

$$P_{x,y,t} = \frac{1}{N}\left[\sum_{x'=x-1}^{x'=x+1}\sum_{y'=y-1}^{y'=y+1}\sum_{t'=t-1}^{t'=t+1}I\left(L_{x',y',t'} = L_{x,y,t}\right)\right] \qquad (3)$$

Where $P_{x,y,t}$ is the homogeneity probability of the pixel in spatial location (x, y) and time point t; usually, the
higher the value of $P_{x,y,t}$, the less the classification error effect. $L_{x,y,t}$ and $L_{x',y',t'}$ are the land-cover labels
of the central pixel and the corresponding spatiotemporal neighboring pixels with a local window of $3 \times 3 \times 3$,
and the $I()$ denotes the indicator function for the equation of the status between two pixels. In this study, the
homogeneity probability was calculated for each changed pixel, and used the threshold of 0.5 (as suggested by
and used in the studies of (Li et al., 2015; Zhang et al., 2022) to judge the rationality of land-cover changes.
Namely, if the $P_{x,y,t}$ was less than the threshold, the $L_{x,y,t}$ would be modified according to the spatiotemporal
pixels.

3.4 Accuracy assessment

The validation process for the GLC_FCS30D dataset follows the recommended guidelines proposed by
Pontus Olofsson (2014). These guidelines encompass two key components: area estimation (nonsite-specific
accuracy) and accuracy assessment (site-specific accuracy). The site-specific accuracy assessment mainly
focuses on estimating the confusion matrix and calculating some accuracy metrics including overall accuracy
(O.A.), producer's accuracy (P.A.), and user's accuracy (U.A.) and the corresponding standard errors using a
poststratified estimator (Pontus Olofsson, 2014). Specifically, because there is currently no global long-time
series validation dataset, we used 84526 global validation points to assess the accuracy metrics of the
GLC_FCS30D dataset in 2020 and used two third-party datasets to analyze the time-series accuracy variations.
The GLC_FCS30D adopts a fine classification system containing 35 subcategories, for which we applied an

analysis protocol into two validation systems (the level-0 classification system containing 10 major land-cover types and the LCCS level-1 validation system containing 17 land-cover types) to comprehensively understand the GLC_FCS30D dataset quality. The correspondence relationship between Level-0 and LCCS level-1

375 validation systems is explained in Table 1.

4. Results and discussion

4.1 Overview of GLC_FCS30D maps and their changes

Figure 4 provides an overview of the GLC_FCS30D dataset in 2022; overall, it aligns with the real-world land-cover patterns on a global scale. Forest, cropland, barren land, and grassland are the dominant land-cover

380 types, and each of them is distributed in the corresponding ecology subregions. For example, needle-leaved forest is mainly concentrated in the high-latitude cold regions while broad-leaved forests are mainly distributed in tropical regions; permanent ice and snow is mainly located in Greenland and high-altitude montains. The GLC_FCS30D has significant advantages over other global land-cover datasets in terms of land-cover type diversity; it contains 35 discrete land-cover types, among which forest and wetland are subdivided into 10 and

385 7 land-cover subcategories, respectively.
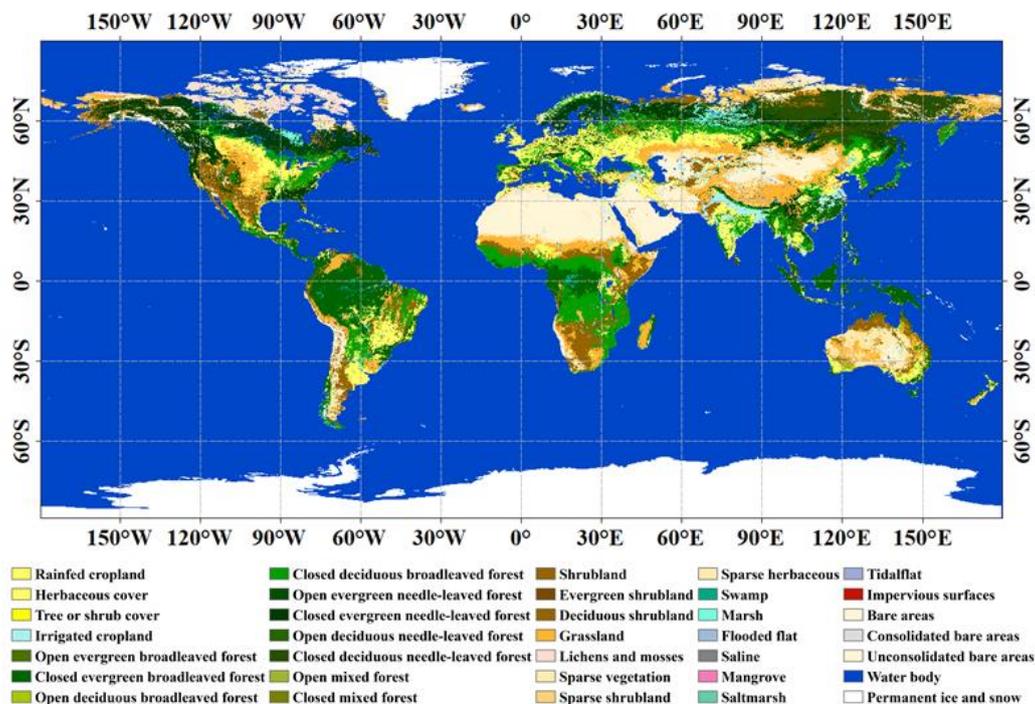
Figure 4. Overview of the GLC_FCS30D in 2022 with a color-coded legend derived from the European Space Agency (ESA) Climate Change Initiative land-cover dataset (Defourny et al., 2018).

Figure 5a illustrates the spatial distribution of land-cover change intensity (measuring the proportions of

390 changed pixels in the 0.05° grid) in the GLC_FCS30D from 1985 to 2022 after upscaling to a resolution of 0.05°. Obviously, global land-cover has experienced significant changes over the past 37 years, mainly in the following three typical areas: 1) tropical rainforest peripheral areas in South America and Southeast Asia, in

which deforestation is the dominant cause; 2) wetland and water-body intermingling areas, such as North America and northern Asia, in which water bodies and wetland were transformed into one another due to different annual water levels. In the GLC_FCS30D the water body land-cover type represents permanent water during the year (it may be wetland in other years). 3) The semi-arid areas in Australia, Central Asia, and western Africa, where land cover (such as sparse vegetation or bare land) is directly affected by precipitation and temperature. For example, if there is sufficient precipitation in the year, the sparse vegetation and some bare land would be covered by grass in semi-arid areas. Similarly, the work of Winkler et al. (2021) revealed that these semi-arid areas experienced serious and frequent land-cover changes. Figure 5b quantitatively counts the changed areas of 10 major land-cover types from 1985 to 2022. Forest and cropland variations dominated global land-cover change. The net loss of forests over the past 37 years reached approximately 2.5 million km^2, and the decline is steady over time. Conversely, cropland showed a stable increase and the net gain in cropland area is approximately 1.3 million km^2. Shrubland, wetland, and impervious surface had increased areas of 0.45 million km^2, 0.40 million km^2, and 0.37 million km^2, respectively. The increased shrubland resulted from the recovery of deforested land, and the wetland gains are due to increases in seasonal water bodies. The work of Pekel et al. (2016) emphasized that the global seasonal water bodies, labeled as inland wetland in the GLC_FCS30D, showed an overall increase.
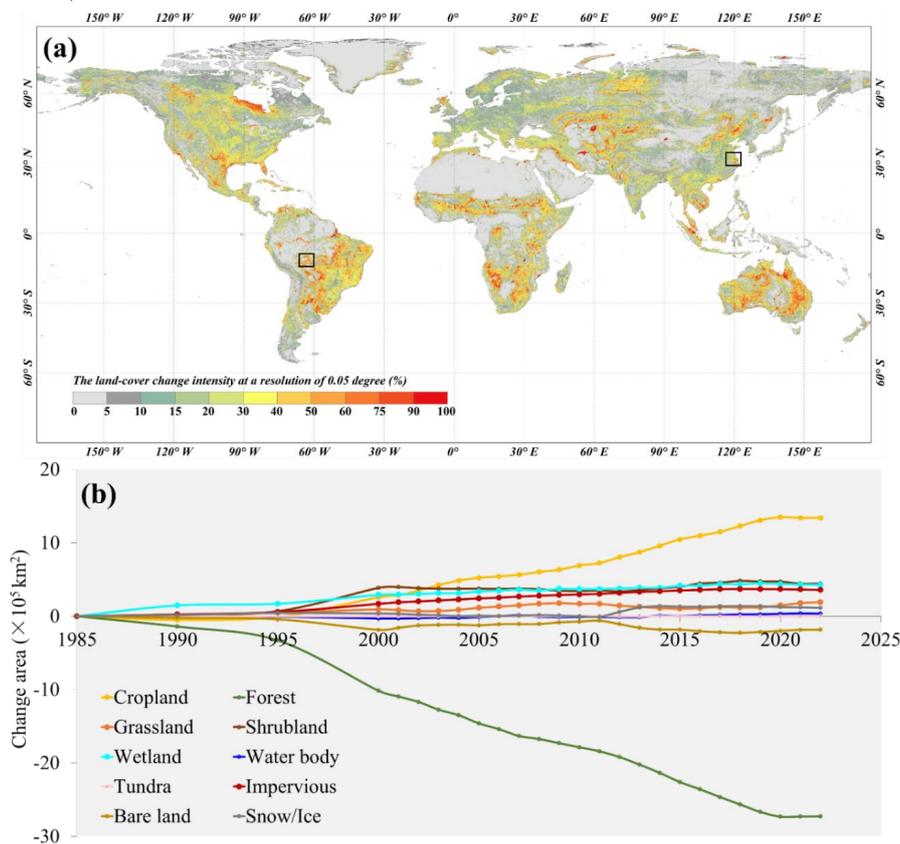
Figure 5. (a) The spatial distribution of global land-cover change intensity from 1985 to 2022 after aggregating to a resolution of 0.05°. (b) The net areas of 10 major land-cover types in GLC_FCS30D from 1985 to 2022.

Figure 6 further analyzes the net area variations of 10 major land-cover types on six continents. The six continents exhibit various land-cover change characteristics, for example, steady forest loss and cropland gain dominate land-cover change in South America, while the net area variations of most land-cover types fluctuate in Australia. North America experiences obvious deforestation, and the forest loss area reaches approximately 4.5×10^5 km^2. In contrast, shrubland, grassland, and impervious surface land-cover types show an overall increasing trend, with increases of 1.4×10^5 km^2, 0.8×10^5 km^2, and 0.72×10^5 km^2, respectively. Similarly, Xian et al. (2022) reported that forest losses and shrubland, grassland, and impervious surface gains are the dominant characteristics of the CONUS from 1985 to 2017. In Europe, the forest area continues to decrease, and the cropland area first decreased and then increased because of the collapse of the Soviet Union in 1990s. Abandoned croplands were transformed into pasture (which also belongs to the cropland land-cover type in the GLC_FCS30D). In Asia, the increase in impervious surface is the most significant across the six continents with a net increase of 1.9×10^5 km^2; wetland also shows a large increase of 1.1×10^5 km^2. The increased wetland coverage comes from the increase in seasonal water bodies. South America and Africa experience similar land-cover change characteristics, with the most intense deforestation rates and the most significant increases in cropland. According to our statistics, the forest loss on these two continents amounts to 16.9×10^5 km^2 and the corresponding increase of cropland is approximately 11.1×10^5 km^2. Last, because Oceania is more sensitive to climate change, especially in terms of precipitation, the fluctuations of shrubland, grassland, and bare land are evident because the conversion relationship between the three land-cover types is related to annual precipitation.
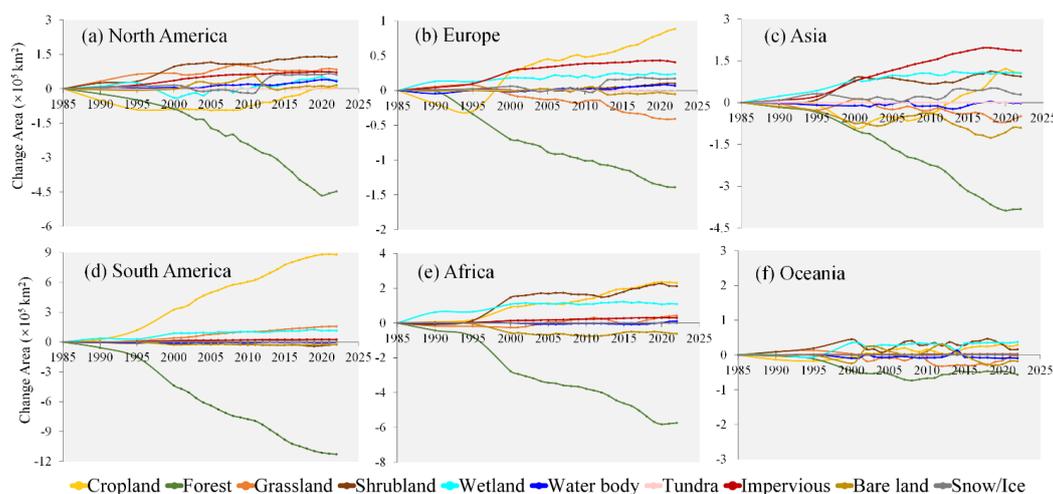
Figure 6. The net area variations of 10 major land-cover types on six continents from 1985 to 2022.

Figure 7 displays the land-cover transformation relationships from 1985 to 2022 in the GLC_FCS30D dataset using Sankey diagrams. Global cropland and forest have obvious area changes and area proportions have changed from 12.08% and 38.26% in 1985 to 12.86% and 36.48% in 2022. Shrubland changed from 8.70% in 1985 to 9.03% in 2022. We mainly focus on forest, cropland, shrubland and impervious surface changes, which dominate the land-cover changes in Figure 5. There are three main causes of forest loss over the past 37 years:

1) 37.58% of deforested land was converted to cropland, which was more significant in tropical rainforest areas (Figure 8a); 2) 26.92% of the lost forest was regrown as shrubland, which is more common in mountainous
440 areas affected by wildfires; and 3) 13.49% of deforested land was converted to grassland. Cropland is converted to forest, grassland, and impervious surface. A total of 26.29% of lost cropland is converted to grassland due to abandonment, 25.88% of lost cropland is covered by forests, and 21.01% of lost cropland resulted from urbanization. Lastly, regarding impervious surface, our primary focus was on identifying the sources contributing to its expansion. Our findings indicate that approximately 36.24% of the impervious surface
445 increase can be attributed to the conversion of cropland, while 13.49% of the increase is a result of deforestation.
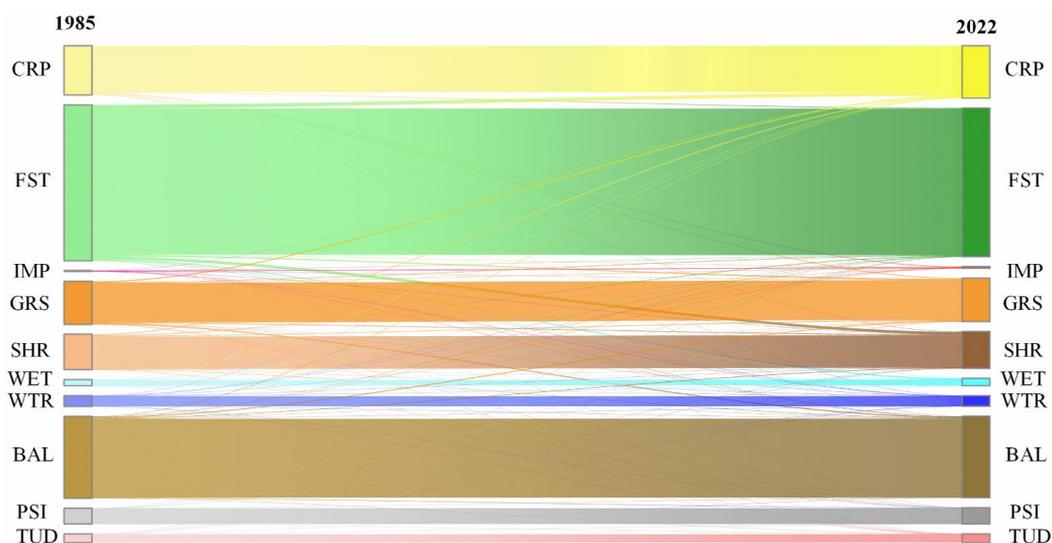
Figure 7. Sankey diagrams of the global land-cover changes during 1985-2022 in the GLC_FCS30D dataset.

To visually understand the land-cover change process captured by the GLC_FCS30D dataset over past 37 years, Figure 8 displays two typical enlargements (spatial location illustrated as two black rectangles in Figure
450 5a) of the Amazon rainforest (which experienced significant deforestation) and China's Yangtze River Delta (which underwent rapid urbanization). These two typical areas experienced drastic land-cover changes and the GLC_FCS30D accurately captures the spatiotemporal changes. In specific, the deforestation in South America is widely recognized, and the GLC_FCS30D clearly reflects this trend. Namely, the early deforestation showed a grid distribution, and then each grid gradually extended outward and finally connected into patches. The
455 GLC_FCS30D also shows that deforestation has not stopped in the region in terms of the rate of forest loss, and these findings are in line with the results of earlier researches (Harris et al., 2021; Potapov et al., 2022). In the Yangtze River Delta, GLC_FCS30D depicts that the dominant land-cover change over the enlargement is urbanization, and a large quantity of irrigated cropland has been converted to impervious surface. Meanwhile, urban expansion was significantly faster before 2010 than after 2010 with the GLC_FCS30D. In short, if we
460 combine real time-series remote-sensing observation data, the GLC_FCS30D effectively captures the spatiotemporal changes of the land surface.
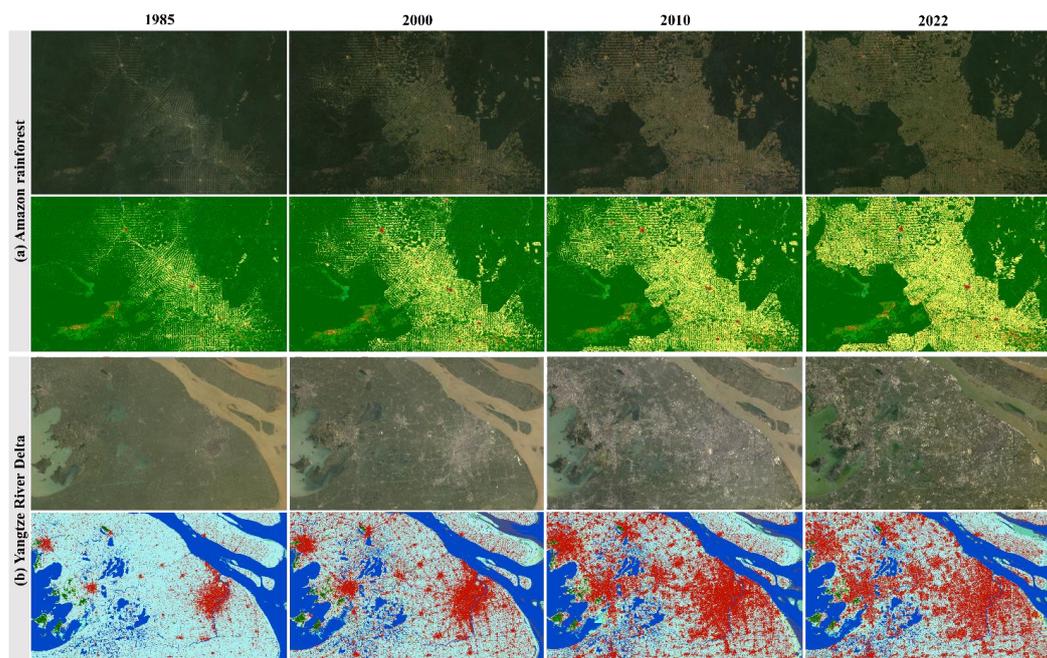
Figure 8. Two typical enlargements of land-cover changes in the GLC_FCS30D from 1985 to 2022 in (a) the Amazon rainforest and (b) the Yangtze River Delta in China. The color-coded legend is like the global map in Figure 4. In each case, the natural-color imagery from 1985 to 2022 is a composite taken from Landsat imagery.

4.2 Accuracy assessment of the GLC_FCS30D in 2020

Table 2 provides the error matrix and accuracy metrics for the GLC_FCS30D dataset in the level-0 classification system containing 10 major land-cover types. The novel GLC_FCS30D dataset attained an overall accuracy of 80.88% (±0.27%). The cropland, forest, impervious surface, water body, as well as permanent snow and ice perform better in terms of the P.A. and U.A. than the remaining land-cover types, with corresponding accuracies exceeding 85%. The impervious surface and wetland datasets are independently generated and then overlaid on the GLC_FCS30D, helping these complicated land-cover types achieve high accuracy metrics. Conversely, grassland, shrubland, and tundra have lower accuracies; for example, grassland had the lowest P.A. of 54.41% and shrubland had the lowest U.A. of 57.63%. The two reasons that they performed poorly were as follows: 1) these land-cover types usually reflected heterogeneous and varied spectral and spatial characteristics, such as the grassland shared similar spectra with cropland and sparse shrubland in the growing season and mimicked bare-land features in harvest season; 2) all of them were distributed in climate-transition areas with complicated climate variations and landscapes.

Table 2. Error matrix of the GLC_FCS30D dataset in 2020 based on the level-0 basic classification system. The reported Producer's Accuracy (P.A.) and User's Accuracy (U.A.) come with their corresponding standard errors (SE) shown in parentheses.

Reference	Map											
	O.A. = 80.88% (±0.27%)											
	CRP	FST	GRS	SHR	WET	WTR	TUD	IMP	BAL	PSI	Total	P.A.(SE)
CRP	15.442	0.792	0.679	0.388	0.086	0.027	0	0.174	0.117	0	17.704	87.22(0.54)

FST	0.513	28.712	0.315	0.811	0.371	0.021	0.008	0.063	0.113	0.002	30.93	92.83(0.31)
GRS	1.035	1.166	5.906	1.181	0.231	0.011	0.084	0.051	1.181	0.01	10.855	54.41(1.02)
SHR	0.555	1.798	0.863	5.392	0.161	0.013	0.019	0.05	0.502	0.002	9.356	57.63(1.09)
WET	0.068	0.465	0.156	0.157	4.047	0.347	0.031	0.021	0.222	0.001	5.516	73.37(1.27)
WTR	0.04	0.086	0.019	0.017	0.302	3.305	0.008	0.012	0.039	0.002	3.831	86.28(1.12)
TUD	0.01	0.123	0.168	0.167	0.018	0.03	2.444	0.002	0.473	0.02	3.454	70.76(1.65)
IMP	0.084	0.058	0.024	0.04	0.001	0.006	0.002	5.043	0.024	0	5.283	95.45(0.61)
BAL	0.13	0.049	0.783	0.585	0.043	0.045	0.577	0.048	9.239	0.131	11.628	79.45(0.8)
PSI	0	0.004	0.03	0.005	0	0.023	0.001	0	0.03	1.351	1.443	93.63(1.38)
Total	17.877	33.251	8.943	8.743	5.259	3.828	3.176	5.464	11.94	1.52		
U.A.(SE)	86.38 (0.55)	86.35 (0.4)	66.05 (1.07)	61.68 (1.11)	76.96 (1.2)	86.33 (1.35)	76.97 (1.6)	92.29 (0.77)	77.38 (0.82)	88.89 (1.72)		

Note: The abbreviations correspond to the 10 categories of the basic classification system in Table 1.

Table 3 provides the error matrix of the GLC_FCS30D in 2020 in the LCCS level-1 validation system with 17 land-cover types. The GLC_FCS30D-2020 dataset achieves an overall accuracy of 73.24% (±0.30%), which

485 is lower than that in the level-0 classification system, because these similar land-cover subcategories more easily suffer from misclassifications. For example, forest has a P.A. of 92.83% (±0.31%) and the P.A. rapidly decreases to the range of 58.29% (±1.53%) to 82.39% (±0.98%) when split into five fine subcategories. Cropland, forest, and bare land, which are further divided into multiple subcategories, show obvious decreases in accuracy over their subcategories in terms of P.A. and U.A. Taking cropland and forest as examples, approximately 31.7% of

490 irrigated cropland (ICP) is misclassified as rainfed cropland (RCP) and so the U.A. of ICP is only 59.92%. More than 53.8% of mixture forests (MFT) are wrongly labeled as the other four forest subcategories and so the mixture forests have the lowest U.A. of 39.34% (±1.38%). Meanwhile, sparse vegetation has the second lowest U.A. of 50.63% (±1.47%) because of the confusion among sparse vegetation, grassland, and bare land. In the level-0 basic classification system (Table 1), sparse vegetation is grouped in with bare land. A previous study

495 in Europe Union proposed grouping it as grassland (Gao et al., 2020). Wetland is further divided into coastal wetland (CWL) and inland wetland (IWL) in Table 3, and the CWL has higher U.A. than that of wetland in Table 2, primarily attributed to its significantly more accurate classification in the CWL (Zhang et al., 2023).

Table 3. Error matrix of the GLC_FCS30D dataset in 2020 based on the LCCS level-1 validation system. The reported Producer's Accuracy (P.A.) and User's Accuracy (U.A.) come with their corresponding standard errors (SE) shown in parentheses.

Reference	RCP	ICP	EBF	DBF	ENF	DNF	MFT	SHR	GRS	LMS	SVG	IWL	CWL	IMP	BAL	WTR	PSI	Total	P.A. (SE)
RCP	12.225	1.023	0.239	0.358	0.102	0.016	0.009	0.382	0.66	0	0.078	0.056	0.005	0.124	0.028	0.001	0	15.332	79.71(0.7)
ICP	0.397	1.932	0.026	0.016	0.005	0	0	0.01	0.025	0	0.012	0.029	0.005	0.052	0	0.018	0	2.527	76.45(1.81)
EBF	0.2	0.048	9.091	1.098	0.262	0.103	0.151	0.371	0.084	0.012	0.012	0.136	0.028	0.029	0	0.004	0	11.514	78.96(0.82)
DBF	0.187	0.016	0.632	6.838	0.537	0.294	0.396	0.235	0.144	0	0.019	0.077	0.002	0.025	0.005	0.004	0.002	9.054	75.53(0.97)
ENF	0.046	0.004	0.174	0.316	5.681	0.328	0.439	0.128	0.034	0.006	0.043	0.094	0	0.002	0.005	0.01	0	6.895	82.39(0.98)
DNF	0.008	0	0.002	0.13	0.245	1.854	0.073	0.071	0.053	0	0.011	0.025	0.001	0.001	0.007	0.002	0	2.414	76.79(1.85)
MFT	0.004	0	0.019	0.176	0.234	0.013	0.828	0.014	0.004	0	0	0.010	0.05	0	0.001	0	0	1.308	58.29(1.53)
SHR	0.518	0.042	0.299	0.9	0.328	0.131	0.034	5.44	0.871	0.019	0.441	0.157	0.005	0.05	0.065	0.013	0.002	9.438	57.63(1.09)
GRS	0.947	0.097	0.167	0.582	0.209	0.154	0.024	1.191	5.958	0.085	0.974	0.229	0.006	0.052	0.217	0.008	0.01	10.95	54.41(1.02)
LMS	0.006	0.004	0.001	0.022	0.044	0.053	0.001	0.168	0.169	2.465	0.379	0.02	0.001	0.002	0.098	0.026	0.02	3.484	70.76(1.65)
SVG	0.064	0.01	0.008	0.006	0.007	0.01	0.001	0.397	0.462	0.025	2.71	0.012	0	0.013	0.643	0.002	0.024	4.399	61.6(1.57)
IWL	0.01	0.002	0.044	0.029	0.103	0.022	0.002	0.048	0.017	0.008	0.042	2.673	0.024	0.001	0.012	0.224	0	3.263	81.91(1.45)
CWL	0.004	0.002	0.008	0.002	0.004	0.002	0.004	0.008	0.006	0	0.008	0.188	1.476	0.007	0.007	0	0	1.783	82.77(1.92)
IMP	0.074	0.011	0.008	0.008	0.037	0.002	0	0.041	0.024	0.002	0.014	0.004	0	5.087	0.01	0.004	0	5.329	95.45(0.61)
BAL	0.048	0.01	0.002	0.004	0.002	0.001	0	0.193	0.328	0.557	0.582	0.043	0.002	0.035	5.384	0.029	0.108	7.33	73.45(1.11)
WTR	0.014	0.024	0.014	0.014	0.019	0.008	0.006	0.011	0.016	0.007	0.011	0.168	0.114	0.011	0.019	3.054	0.002	3.509	87.04(1.22)
PSI	0	0	0	0.001	0.002	0	0	0.005	0.03	0.001	0.011	0	0	0	0.019	0.023	1.363	1.455	93.65(1.37)
Total	14.757	3.224	10.753	10.56	7.833	3.724	1.97	8.711	8.883	3.179	5.353	3.927	1.668	5.497	6.526	3.482	1.532		
U.A.	82.85	59.92	84.55	64.76	72.52	49.77	39.34	62.44	67.07	77.55	50.63	68.07	88.49	92.54	82.5	87.73	88.96		
U.A. (SE)	(0.67)	(1.85)	(1.75)	(1)	(1.08)	(1.76)	(1.38)	(1.11)	(1.07)	(1.59)	(1.47)	(1.6)	(1.68)	(0.76)	(1.01)	(1.19)	(1.72)		
O.A.									73.04% (±0.30%)										

Note: The abbreviations correspond to the 17 categories of the LCCS validation system in Table 1.

4.3 Accuracy assessment based on two third-party regional validation datasets

4.3.1 Time-series accuracy metrics of GLC_FCS30D from LCMAP_Val dataset

Figure 9 displays time-series variations of the overall accuracy of the GLC_FCS30D dataset using the LCMAP_Val annual validation dataset from 1985 to 2018 over the CONUS. The GLC_FCS30D achieves a mean overall accuracy of 79.50% ($\pm$0.50%) and varies from a high value of 80.04% ($\pm$0.49%) in 2015 to a low value of 78.91% ($\pm$0.51%) in 2000. The overall accuracy of GLC_FCS30D is slightly lower at the early stage, which might be related to the density of Landsat observations. The early Landsat missions had weaker satellite-to-ground transmission and onboard recording capabilities (Roy et al., 2014a), so phenological variability and land-cover changes were more difficult to capture in the early stage.
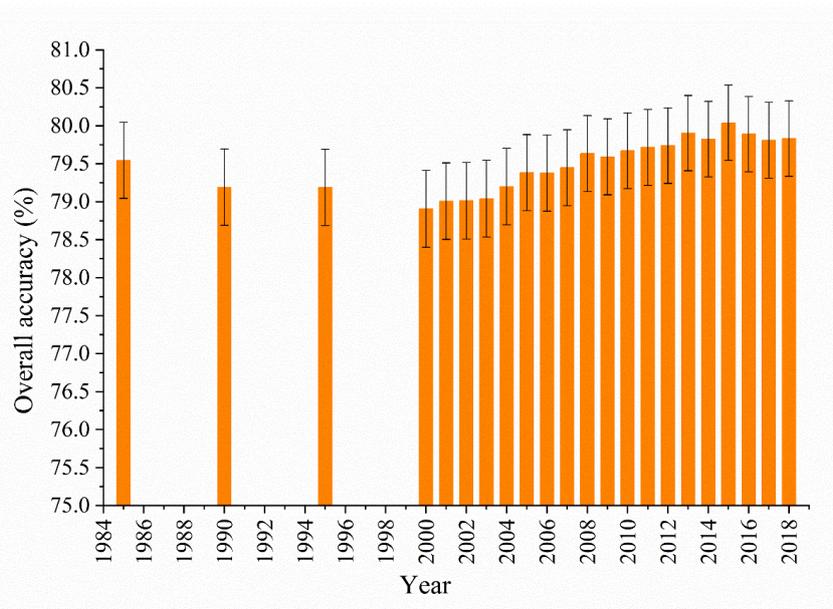
Figure 9. The time-series overall accuracy of the GLC_FCS30D dataset using the LCMAP_Val annual reference dataset across the contiguous United States (CONUS) from 1985 to 2018. The error bars on the graph show the uncertainty of each data point.

Figure 10 further illustrates the time-series variations of P.A. and U.A. for the GLC_FCS30D dataset in the CONUS. Visually, the P.A. and U.A. of 10 major land-cover types range from 45% to 100% and 35% to 100%, respectively, and the time-series variations are stable. Among them, the water body land-cover type has the highest accuracy metrics, achieving mean P.A. and U.A. values of 95.31% ($\pm$1.14%) and 98.53% ($\pm$0.66%), respectively, which benefit from its unique spectral characteristics. Cropland follows with mean P.A. and U.A. values of 93.37% ($\pm$0.74%) and 87.70% ($\pm$0.94%), respectively. Forest ranks third with a high P.A. of 97.75% ($\pm$0.35%) but relatively low U.A. of 82.42% ($\pm$0.82%); the unbalanced metrics are because GLC_FCS30D and LCMAP_Val have different definitions for forest. GLC_FCS30D defines the tree cover of the forest as greater than 15% and the threshold setting of LCMAP_Val is 10%, so many shrublands in the GLC_FCS30D are labeled as forest in the LCMAP_Val. Wetland has a U.A. value of 90.47% ($\pm$2.05%) but a

P.A. value of 57.07% (±2.75%), which is also caused by a discrepancy in the definition of wetland. GLC_FCS30D identifies seasonal water bodies as wetland while the LCMAP_Val classifies them as water body.

525 Impervious surface has a P.A. lower than 60% mainly because the GLC_FCS30D and LCMAP_Val datasets have different definitions of impervious surface. LCMAP_Val defines buildings and the surrounding green areas as developed, while GLC_FCS30D only includes the artificial buildings (houses, roads, squares, and so on). Bare land and shrubland have the lowest U.A. values of 35.58% (±4.39%) and 47.29% (±1.56%), respectively, mainly because both of them are easily confused with grassland due to the complicated spectral characteristics

530 and coexist in climate-sensitive semi-arid regions (e.g., the Midwestern United States). Xian et al. (2022) emphasized that long-term monitoring of shrubs and grasslands presents significant challenges in the CONUS. Permanent snow and ice, which is sparsely distributed in high-elevation mountainous areas of the United States, has unique and specific spectral characteristics, so it achieves 100% P.A. in the GLC_FCS30D. The large fluctuations in U.A. are because the LCMAP_Val dataset has a small sample size for ice and snow and the

535 commission error of other land-cover types causes large variations.
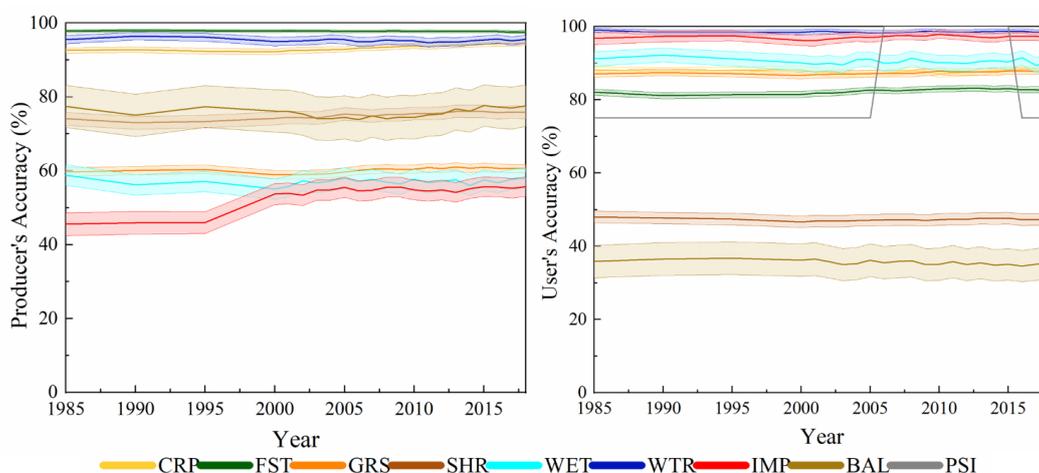
Figure 10. The time-series producer's accuracy and user's accuracy of GLC_FCS30D based on the LCMAP_Val dataset from 1985 to 2018 in the contiguous United States (CONUS). The error band represents ±1 standard errors.

540 Figure 11 indicates the area-bias percentage of eight land-cover types estimated by GLC_FCS30D and LCMAP_Val across the CONUS. Intuitively, the GLC_FCS30D and LCMAP_Val share similar total areas for estimation of cropland, bare land, and water body, and show evident area deviations for estimating forest, shrubland, and grassland. The deviations in shrubland and grassland are mainly because these land-cover types coexist in the semi-arid regions of the central United States and share similar spectral characteristics and

545 temporal variability; thus, some grasslands in the LCMAP_Val are considered as shrubland in the GLC_FCS30D. Xian et al. (2022) also failed to distinguish grassland and shrubland and combined them as a group in generating the LCMAP annual maps. The LCMAP_Val has a broader definition of impervious surface and resulting negative bias, so the impervious surface area estimated in LCMAP_Val is larger than the assessment in GLC_FCS30D dataset.
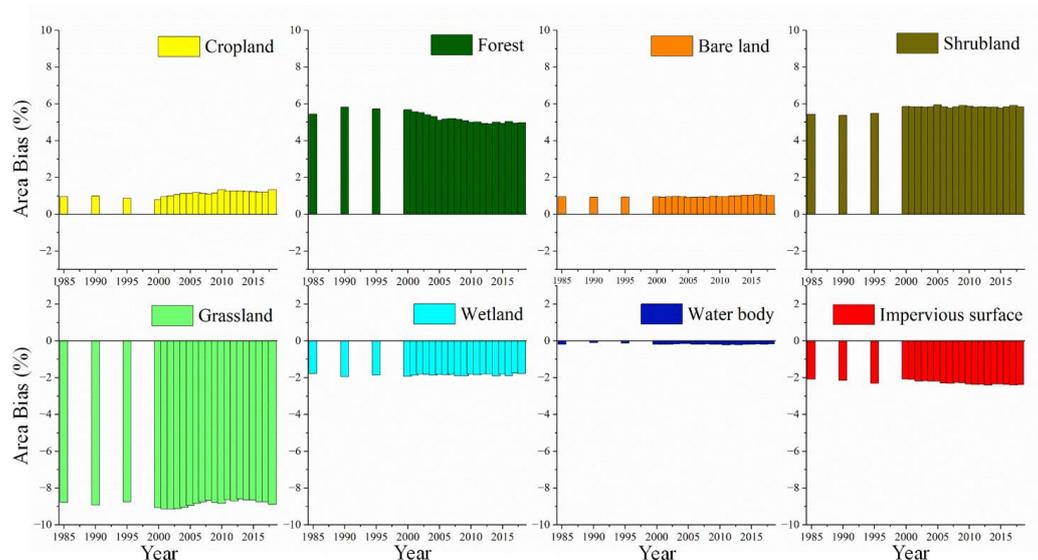
550

Figure 11. The area-bias percentage of eight land-cover types in the GLC_FCS30D and LCMAP_Val datasets
from 1985 to 2017 in the contiguous United States (CONUS).

4.3.2 Time-series accuracy metrics of GLC_FCS30D from the LUCAS dataset

Table 4 lists the time-series accuracy metrics of the GLC_FCS30D dataset across the European Union (EU)

555   from 2006 to 2018 using the LUCAS dataset. The GLC_FCS30D dataset has a mean overall accuracy of 81.91%
(±0.09%) ranging from 81.64% (0.09%) to 82.11% (0.09%) in EU. The two dominant land-cover types
(cropland and forest) that cover almost 70% of the entire EU area (Gao et al., 2020)) have higher P.A. and U.A.
values than other land-cover types. The P.A. and U.A. of cropland exceed 85% and 93%, respectively. Forest
has unbalanced P.A. (approximately 95%) and U.A. values (approximately 76%) because the LUCAS dataset

560   defines forest more broadly than the GLC_FCS30D dataset. In specific, sparse vegetation associated with forest
is grouped as forest in LUCAS but as bare land in GLC_FCS30D. Gao et al. (2020) explained the discrepancy
in the forest definition between LUCAS and GLC_FCS30. Shrubland, grassland, and bare land showed inferior
performance in both P.A. and U.A. because of their complicated spectral variability and spatial heterogeneity.
Gao et al. (2020) also found that three global 30-m land-cover products (GlobeLand30, FROM_GLC, and

565   GLC_FCS30) exhibited poor performance for these three land-cover types. Urban green space and
discontinuous urban fabric, excluding from the GLC_FCS30D, are grouped as impervious surface in the
LUCAS. Thus, the impervious surface also has a low P.A. of approximately 59%. Last, we further investigate
the temporal variability of P.A. and U.A. and find that permanent ice and snow and wetland show greater
variability and that both are closely related to annual temperature and precipitation; namely, their spatial

570   distributions are affected by the natural environment.

Table 4. Time-series accuracy metrics of the GLC_FCS30D dataset using the LUCAS validation dataset across
the European Union.

	2006		2009		2012		2015		2018	
	P.A.(SE)	U.A.(SE)	P.A.(SE)	U.A.(SE)	P.A.(SE)	U.A.(SE)	P.A.(SE)	U.A.(SE)	P.A.(SE)	U.A.(SE)

CRP	85.49(0.11)	93.37(0.08)	85.40(0.11)	93.31(0.08)	85.50(0.11)	93.17(0.08)	85.47(0.11)	93.05(0.08)	85.52(0.11)	92.82(0.08)
FST	95.22(0.08)	76.71(0.15)	94.97(0.08)	76.71(0.15)	94.79(0.09)	76.82(0.15)	94.36(0.09)	76.82(0.15)	93.71(0.09)	76.85(0.15)
GRS	6.13(0.26)	21.31(0.83)	6.10(0.26)	21.13(0.83)	6.05(0.26)	20.98(0.83)	6.08(0.26)	20.71(0.82)	5.99(0.26)	20.74(0.82)
SHR	8.13(0.42)	8.93(0.46)	8.25(0.43)	8.92(0.46)	8.02(0.42)	8.77(0.46)	7.84(0.42)	8.60(0.45)	8.35(0.43)	8.96(0.46)
WET	63.10(0.81)	66.55(0.81)	61.40(0.81)	65.55(0.82)	61.86(0.81)	66.21(0.82)	62.64(0.81)	66.60(0.81)	62.94(0.81)	65.34 (0.81)
WTR	89.73(0.40)	92.44(0.36)	90.09(0.40)	92.53(0.35)	90.28(0.39)	92.36(0.36)	90.83(0.38)	91.63(0.37)	90.10(0.40)	91.56(0.37)
IMP	58.55(0.56)	72.69(0.56)	59.21(0.55)	72.06(0.56)	59.06(0.55)	71.72(0.56)	58.65(0.55)	70.85(0.56)	59.01(0.55)	70.29(0.56)
BAL	52.77(1.12)	39.62(0.95)	52.90(1.12)	38.44(0.93)	52.19(1.13)	37.70(0.93)	52.07(1.13)	36.16(0.90)	52.33(1.13)	34.69(0.87)
PSI	86.02(5.00)	35.01(4.38)	91.40(4.04)	36.56(4.38)	89.25(4.46)	31.86(4.00)	96.24(2.74)	31.40(3.81)	96.24(2.74)	31.35(3.81)
O.A.(SE)	82.11(0.09)		81.99(0.09)		81.97(0.09)		81.82(0.09)		81.64(0.09)	

Table 5 shows the area proportions of 10 major land-cover types from the GLC_FCS30D dataset (Map) and LUCAS validation dataset (Ref), respectively. The area bias (AB) measures the area deviations of the two different datasets for the same land-cover type. Overall, the GLC_FCS30D overestimates the total area assessments of forest, bare land, and ice and snow, and underestimates the remaining land-cover types in comparison to the LUCAS estimations. In particular, the AB of forest is the most significant overestimation of +7.356%, and the underestimated MB of cropland is −4.086%. Cropland and forest cover together account for approximately 70% of the total EU area (Gao et al., 2020)), as a result, the area bias (AB) values for these two land-cover types are more noticeable or pronounced compared to the AB values of the other land-cover types.

Table 5. The area proportions and area bias (AB) values of 10 major land-cover types from the GLC_FCS30D dataset (Map) and the LUCAS validation dataset (Ref).

	2006			2009			2012			2015			2018		
	Map	Ref	AB	Map	Ref	AB	Map	Ref	AB	Map	Ref	AB	Map	Ref	AB
CRP	46.48	50.62	-4.14	46.46	50.64	-4.18	46.59	50.67	-4.08	46.63	50.69	-4.06	46.77	50.74	-3.97
FST	41.39	33.76	7.63	41.28	33.75	7.53	41.14	33.73	7.41	40.96	33.73	7.23	40.66	33.68	6.98
GRS	1.21	4.15	-2.94	1.21	4.15	-2.94	1.21	4.15	-2.94	1.23	4.15	-2.92	1.21	4.15	-2.94
SHR	1.91	2.08	-0.17	1.94	2.08	-0.14	1.92	2.08	-0.16	1.91	2.07	-0.16	1.95	2.06	-0.11
WET	1.70	1.75	-0.05	1.68	1.74	-0.06	1.68	1.73	-0.05	1.69	1.71	-0.02	1.73	1.72	0.01
WTR	2.75	2.85	-0.1	2.76	2.85	-0.09	2.77	2.85	-0.08	2.81	2.85	-0.04	2.79	2.86	-0.07
IMP	3.18	3.82	-0.64	3.25	3.83	-0.58	3.25	3.82	-0.57	3.27	3.82	-0.55	3.32	3.82	-0.5
BAL	1.32	0.95	0.37	1.36	0.95	0.41	1.37	0.95	0.42	1.42	0.95	0.47	1.49	0.95	0.54
PSI	0.06	0.02	0.04	0.06	0.02	0.04	0.07	0.02	0.05	0.07	0.02	0.05	0.07	0.02	0.05

4.4 Limitations and perspectives of the GLC_FCS30D dataset

To achieve the goal of accurate and robust monitoring of global land-cover change, four steps are adopted: 1) combining the advantages of the CCD model and full time-series Landsat observations to capture the land-cover change time-points for any changed pixels; 2) using the temporally stable areas as prior knowledge to ensure the quality of training samples and adopting local adaptive modeling to update the land-cover transitions of these changed pixels; 3) independently developing global thematic products for two complicated land-cover types (impervious surface and wetland) to improve the reliability of the GLC_FCS30D; and 4) applying the 'spatiotemporal consistency checking' optimization in Section 3.3.3 to further guarantee the stability and accuracy of the GLC_FCS30D. The accuracy assessments, using the developed global validation dataset and

two third-party datasets, demonstrate that the GLC_FCS30D fulfills accuracy requirements at a baseline year and for time-series variability over global or national scales. Comparisons with other land-cover products also highlight the superiority of the GLC_FCS30D in terms of classification system diversity and monitoring
595 accuracy of these changed-areas. However, long time-series monitoring of global land-cover change is an extremely complex and difficult task (Hansen and Loveland, 2012; Song et al., 2018; Winkler et al., 2021; Xian et al., 2022). Although this study takes a series of measurements and methods to achieve global 30-m land cover change monitoring over past 37 years, there are still some uncertainties and limitations that need to be resolved in further work.

600 The CCD algorithm makes full use of dense satellite observations to capture land-cover changes robustly and accurately (Zhu and Woodcock, 2014b; Zhu et al., 2012). However, previous studies have demonstrated that their reliability is highly correlated to the density of valid satellite observations (Bullock et al., 2022; Ye et al., 2021; Zhu et al., 2019). Cloudy and snowy areas have greater uncertainty for capturing the time points of land-cover change (DeVries et al., 2015; Xian et al., 2022). Additionally, due to the limited storage capacity
605 and satellite–ground data-transmission capacity of early satellites, the density of Landsat imagery is sparse before 2000 (only Landsat 5 single-satellite acquired data) (Roy et al., 2014b). In this study, we combine the satellite observations from two years before and after the nominal center year from 1985 to 1995; for example, we update the land-cover maps in 1995 using all available imagery from 1993 to 1997. However, a previous study found that northeastern Asia did not have any valid Landsat observations before 2000 (Zhang et al., 2022),
610 which means some land-cover changes could not be captured in the GLC_FCS30D in these areas before 2000. To solve the problem of missing and sparse observations, a useful solution is to fuse multisourced remote-sensing imagery. For example, Zhang et al. (2021c) combined Landsat and Sentinel-2 imagery to track tropical forest disturbances with overall accuracy of more than 87%. Therefore, further work will investigate the feasibility of integrating Sentinel 1/2, MODIS, and AVHRR imagery as auxiliary datasets.

615 GLC_FCS30D reveals a large number of land-cover changes in the semi-arid regions illustrated in Figure 5a, in which the land-cover changes are more influenced by climate factors. For example, the central region of Australia is a typical semi-arid region, and the dominant land-cover types are grassland, sparse vegetation, shrubland, and bare land. In general, if there is sufficient annual precipitation, the distributions of shrubland and grassland in the area will be more extensive; otherwise the area will be dominated by bare land and sparse
620 vegetation (Dong et al., 2020; Ge et al., 2022). Recently, some studies suggested suppressing these changes; for example, Bastos et al. (2022) chose to suppress these land-cover changes by fusing these four land-cover types into the single grassland land-cover type in Australia, and Xian et al. (2022) combined grassland and shrubland together in the CONUS. Whether these frequent and climate-sensitive land-cover changes should be suppressed will be considered in our further work.

625 Although we used a global validation dataset to assess the capability of GLC_FCS30D in the baseline year of 2020 and two third-party regional datasets to assess its time-series accuracy variability in the European Union and the CONUS, the accuracy assessment work should be strengthened. In specific, the classification system differences among GLC_FCS30D, LUCAS, and LCMAP_Val cannot be ignored. For example, the impervious surface land-cover type in the LUCAS and LCMAP_Val contains artificial surfaces and their surroundings (such
630 as city greenery) (Stehman et al., 2021; Xian et al., 2022), while the GLC_FCS30D only includes artificial structures (Zhang et al., 2022), so the impervious surface in GLC_FCS30D has low P.A. when validating with the LUCAS and LCMAP_Val datasets in Section 4.3. The time-series accuracy variability is only analyzed in

two regions, so its performance in more complex areas (such as Africa) needs to be further studied. Thus, our future work would collect long-term time-series validation data sets for more regions and build a long time-series global validation dataset based on the existing works in Section 2.5.1.

5. Data availability

The developed GLC_FCS30D dataset can be freely accessible via https://doi.org/10.5281/zenodo.8239305 (Liu et al, 2023). To allow users to better select this dataset, it is saved as 961 5° × 5° independent tiles. Each tile is named as 'GLC_FCS30D_yyyyYYYY_E/W**N/S**.tif', in which 'E/W**N/S**' represents the longitude and latitude coordinates of the top-left corner, and yyyy and YYYY are the start and end years of the land-cover change monitoring. The GLC_FCS30D contains 26 time-step maps from 1985 to 2022, updated every five years before 2000 and annually from 2000 to 2022The first three time steps are saved together and the following 23 time steps are saved separately. For example, GLC_FCS30D_19851995_E115N15.tif and GLC_FCS30D_20002022_E115N15.tif are the first three time-steps and the following 23 annual time-steps data from 1985 to 2022 for the region of 115°–120°E, 10°–15°N, respectively.

6. Conclusion

Land cover change is the main cause or driving force of global climate change and has attracted increasing attention over the past decades. Long time-series global land-cover dynamic monitoring is still a challenging task. In this study, the first global 30-m land-cover dynamic dataset with fine classification system (GLC_FCS30D), containing 35 fine land-cover sub-categories and covering the period of 1985 to 2022 with 26 time-steps, is generated on the GEE platform. In specific, we take advantage of the full time-series Landsat observations and the CCD algorithm to capture the time-points of changed areas, and then update and optimize the land-cover changed areas based on the local adaptive modeling strategy and a temporal-consistency algorithm. The accuracy assessments indicate that the proposed method can achieve accurate and spatiotemporally consistent land-cover change monitoring, and the GLC_FCS30D achieves an overall accuracy in 2020 of 80.88% ($\pm$0.27%) for the basic classification system 10 major land-cover types) and 73.24% ($\pm$0.30%) for the LCCS level-1 validation system (17 LCCS land-cover types). Therefore, the GLC_FCS30D is the first global land-cover dynamic monitoring product with a 37-year time span and the most diverse classification system. It will be essential for sustainable development, environmental protection, and informed decision-making to address the challenges of a rapidly changing world.

Financial support

This research has been supported by the Open Research Program of the International Research Center of Big Data for Sustainable Development Goals (grant no. CBAS2022ORP03) and the National Natural Science Foundation of China (grant no. 42201499).

Author contributions

LL and XZ conceptualized and investigated the project. XZ, TZ, XC designed the methodology, TZ, WL, HT and JW performed the validation. XZ prepared the original draft of the paper, LL and HT reviewed and edited the paper.

Competing interests

670 The authors declare that they have no conflict of interest.

References

Azzari, G. and Lobell, D. B.: Landsat-based classification in the cloud: An opportunity for a paradigm shift in land cover monitoring, Remote Sensing of Environment, 202, 64-74, https://doi.org/10.1016/j.rse.2017.05.025, 2017.

675 Büttner, G. and Eiselt, B.: LUCAS and CORINE Land Cover. EEA and Eurostat Luxembourg, 2013.

Ballin, M., Barcaroli, G., Masselli, M., and Scarnò, M.: Redesign sample for land use/cover area frame survey (LUCAS) 2018, Eurostat: statistical working papers. 10, 132365, available at: https://ec.europa.eu/eurostat/web/products-statistical-working-papers/-/KS-TC-18-006 (last access: 4 August 2023), 2018.

680 Ban, Y., Gong, P., and Giri, C.: Global land cover mapping using Earth observation satellite data: Recent progresses and challenges, ISPRS Journal of Photogrammetry and Remote Sensing, 103, 1-6, https://doi.org/10.1016/j.isprsjprs.2015.01.001, 2015.

Bastos, A., Ciais, P., Sitch, S., Aragao, L., Chevallier, F., Fawcett, D., Rosan, T. M., Saunois, M., Gunther, D., Perugini, L., Robert, C., Deng, Z., Pongratz, J., Ganzenmuller, R., Fuchs, R., Winkler, K., Zaehle, S., and

685 Albergel, C.: On the use of Earth Observation to support estimates of national greenhouse gas emissions and sinks for the Global stocktake process: lessons learned from ESA-CCI RECCAP2, Carbon Balance Manag, 17, 15, https://doi.org/10.1186/s13021-022-00214-w, 2022.

Belgiu, M. and Drăguţ, L.: Random forest in remote sensing: A review of applications and future directions, ISPRS Journal of Photogrammetry and Remote Sensing, 114, 24-31,

690 https://doi.org/10.1016/j.isprsjprs.2016.01.011, 2016.

Bullock, E. L., Healey, S. P., Yang, Z., Houborg, R., Gorelick, N., Tang, X., and Andrianirina, C.: Timeliness in forest change monitoring: A new assessment framework demonstrated using Sentinel-1 and a continuous change detection algorithm, Remote Sensing of Environment, 276, 113043, https://doi.org/10.1016/j.rse.2022.113043, 2022.

695 Bullock, E. L., Woodcock, C. E., and Holden, C. E.: Improved change monitoring using an ensemble of time series algorithms, Remote Sensing of Environment, 111165, https://doi.org/10.1016/j.rse.2019.04.018, 2019.

d'Andrimont, R., Yordanov, M., Martinez-Sanchez, L., Eiselt, B., Palmieri, A., Dominici, P., Gallego, J., Reuter, H. I., Joebges, C., and Lemoine, G.: Harmonised LUCAS in-situ land cover and use database for field surveys from 2006 to 2018 in the European Union, Scientific data, 7, 352, https://doi.org/10.1038/s41597-020-00675-z,

700 2020.

Defourny, P., Kirches, G., Brockmann, C., Boettcher, M., Peters, M., Bontemps, S., Lamarche, C., Schlerf, M., and M., S.: Land Cover CCI: Product User Guide Version 2, available at: https://www.esa-landcover-cci.org/?q=webfm_send/84 (last access: 4 August 2023), 2018.

DeVries, B., Verbesselt, J., Kooistra, L., and Herold, M.: Robust monitoring of small-scale forest disturbances

705 in a tropical montane forest using Landsat time series, Remote Sensing of Environment, 161, 107-121, https://doi.org/10.1016/j.rse.2015.02.012, 2015.

Dong, J., Xiao, X., Kou, W., Qin, Y., Zhang, G., Li, L., Jin, C., Zhou, Y., Wang, J., Biradar, C., Liu, J., and Moore, B.: Tracking the dynamics of paddy rice planting area in 1986–2010 through time series Landsat images

and phenology-based algorithms, Remote Sensing of Environment, 160, 99-113,
710 https://doi.org/10.1016/j.rse.2015.01.004, 2015.

Dong, S., Shang, Z., Gao, J., and Boone, R. B.: Enhancing sustainability of grassland ecosystems through
ecological restoration and grazing management in an era of climate change on Qinghai-Tibetan Plateau,
Agriculture, Ecosystems & Environment, 287, 106684, https://doi.org/10.1016/j.agee.2019.106684, 2020.

Foley, J. A., Defries, R., Asner, G. P., Barford, C., Bonan, G., Carpenter, S. R., Chapin, F. S., Coe, M. T., Daily,
715 G. C., Gibbs, H. K., Helkowski, J. H., Holloway, T., Howard, E. A., Kucharik, C. J., Monfreda, C., Patz, J. A.,
Prentice, I. C., Ramankutty, N., and Snyder, P. K.: Global consequences of land use, Science, 309, 570-574,
https://doi.org/10.1126/science.1111772, 2005.

Foody, G. M.: Sample size determination for image classification accuracy assessment and comparison,
International Journal of Remote Sensing, 30, 5273-5291, https://doi.org/10.1080/01431160903130937, 2009.

720 Foody, G. M. and Arora, M. K.: An evaluation of some factors affecting the accuracy of classification by an
artificial neural network, International Journal of Remote Sensing, 18, 799-810,
https://doi.org/10.1080/014311697218764, 2010.

Friedl, M. A., Sulla-Menashe, D., Tan, B., Schneider, A., Ramankutty, N., Sibley, A., and Huang, X.: MODIS
Collection 5 global land cover: Algorithm refinements and characterization of new datasets, Remote Sensing of
725 Environment, 114, 168-182, https://doi.org/10.1016/j.rse.2009.08.016, 2010.

Friedl, M. A., Woodcock, C. E., Olofsson, P., Zhu, Z., Loveland, T., Stanimirova, R., Arevalo, P., Bullock, E.,
Hu, K.-T., Zhang, Y., Turlej, K., Tarrio, K., McAvoy, K., Gorelick, N., Wang, J. A., Barber, C. P., and Souza,
C.: Medium Spatial Resolution Mapping of Global Land Cover and Land Cover Change Across Multiple
Decades From Landsat, Frontiers in Remote Sensing, 3, https://doi.org/10.3389/frsen.2022.894571, 2022.

730 Friedlingstein, P., O'Sullivan, M., Jones, M. W., Andrew, R. M., Hauck, J., Olsen, A., Peters, G. P., Peters, W.,
Pongratz, J., Sitch, S., Le Quéré, C., Canadell, J. G., Ciais, P., Jackson, R. B., Alin, S., Aragão, L. E. O. C.,
Arneth, A., Arora, V., Bates, N. R., Becker, M., Benoit-Cattin, A., Bittig, H. C., Bopp, L., Bultan, S., Chandra,
N., Chevallier, F., Chini, L. P., Evans, W., Florentie, L., Forster, P. M., Gasser, T., Gehlen, M., Gilfillan, D.,
Gkritzalis, T., Gregor, L., Gruber, N., Harris, I., Hartung, K., Haverd, V., Houghton, R. A., Ilyina, T., Jain, A.
735 K., Joetzjer, E., Kadono, K., Kato, E., Kitidis, V., Korsbakken, J. I., Landschützer, P., Lefèvre, N., Lenton, A.,
Lienert, S., Liu, Z., Lombardozzi, D., Marland, G., Metzl, N., Munro, D. R., Nabel, J. E. M. S., Nakaoka, S.-I.,
Niwa, Y., O'Brien, K., Ono, T., Palmer, P. I., Pierrot, D., Poulter, B., Resplandy, L., Robertson, E., Rödenbeck,
C., Schwinger, J., Séférian, R., Skjelvan, I., Smith, A. J. P., Sutton, A. J., Tanhua, T., Tans, P. P., Tian, H.,
Tilbrook, B., van der Werf, G., Vuichard, N., Walker, A. P., Wanninkhof, R., Watson, A. J., Willis, D., Wiltshire,
740 A. J., Yuan, W., Yue, X., and Zaehle, S.: Global Carbon Budget 2020, Earth Syst. Sci. Data, 12, 3269-3340,
https://doi.org/10.5194/essd-12-3269-2020, 2020.

Gallant, A.: The Challenges of Remote Monitoring of Wetlands, Remote Sensing, 7, 10938-10950,
https://doi.org/10.3390/rs70810938, 2015.

Gao, Y., Liu, L., Zhang, X., Chen, X., Mi, J., and Xie, S.: Consistency Analysis and Accuracy Assessment of
745 Three Global 30-m Land-Cover Products over the European Union using the LUCAS Dataset, Remote Sensing,
12, 3479, https://doi.org/10.3390/rs12213479, 2020.

Ge, F., Xu, M., Gong, C., Zhang, Z., Tan, Q., and Pan, X.: Land cover changes the soil moisture response to
rainfall on the Loess Plateau, Hydrological Processes, 36, https://doi.org/10.1002/hyp.14714, 2022.

Giri, C., Pengra, B., Long, J., and Loveland, T. R.: Next generation of global land cover characterization, mapping, and monitoring, International Journal of Applied Earth Observation and Geoinformation, 25, 30-37, https://doi.org/10.1016/j.jag.2013.03.005, 2013.

Gislason, P. O., Benediktsson, J. A., and Sveinsson, J. R.: Random Forests for land cover classification, Pattern Recognition Letters, 27, 294-300, https://doi.org/10.1016/j.patrec.2005.08.011, 2006.

Gong, P., Li, X., and Zhang, W.: 40-Year (1978–2017) human settlement changes in China reflected by impervious surfaces from satellite remote sensing, Science Bulletin, 64, 756-763, https://doi.org/10.1016/j.scib.2019.04.024, 2019.

Gorelick, N., Hancher, M., Dixon, M., Ilyushchenko, S., Thau, D., and Moore, R.: Google Earth Engine: Planetary-scale geospatial analysis for everyone, Remote Sensing of Environment, 202, 18-27, https://doi.org/10.1016/j.rse.2017.06.031, 2017.

Hansen, M. C. and Loveland, T. R.: A review of large area monitoring of land cover change using Landsat data, Remote Sensing of Environment, 122, 66-74, https://doi.org/10.1016/j.rse.2011.08.024, 2012.

Hansen, M. C., Potapov, P. V., Moore, R., Hancher, M., Turubanova, S. A., Tyukavina, A., Thau, D., Stehman, S. V., Goetz, S. J., Loveland, T. R., Kommareddy, A., Egorov, A., Chini, L., Justice, C. O., and Townshend, J. R.: High-resolution global maps of 21st-century forest cover change, Science, 342, 850-853, https://doi.org/10.1126/science.1244693, 2013.

Harris, N. L., Gibbs, D. A., Baccini, A., Birdsey, R. A., de Bruin, S., Farina, M., Fatoyinbo, L., Hansen, M. C., Herold, M., Houghton, R. A., Potapov, P. V., Suarez, D. R., Roman-Cuesta, R. M., Saatchi, S. S., Slay, C. M., Turubanova, S. A., and Tyukavina, A.: Global maps of twenty-first century forest carbon fluxes, Nature Climate Change, 11, 234-240, https://doi.org/10.1038/s41558-020-00976-6, 2021.

Healey, S. P., Cohen, W. B., Yang, Z., Kenneth Brewer, C., Brooks, E. B., Gorelick, N., Hernandez, A. J., Huang, C., Joseph Hughes, M., Kennedy, R. E., Loveland, T. R., Moisen, G. G., Schroeder, T. A., Stehman, S. V., Vogelmann, J. E., Woodcock, C. E., Yang, L., and Zhu, Z.: Mapping forest change using stacked generalization: An ensemble approach, Remote Sensing of Environment, 204, 717-728, https://doi.org/10.1016/j.rse.2017.09.029, 2018.

Herold, M., Mayaux, P., Woodcock, C. E., Baccini, A., and Schmullius, C.: Some challenges in global land cover mapping: An assessment of agreement and accuracy in existing 1 km datasets, Remote Sensing of Environment, 112, 2538-2556, https://doi.org/10.1016/j.rse.2007.11.013, 2008.

Homer, C., Dewitz, J., Jin, S., Xian, G., Costello, C., Danielson, P., Gass, L., Funk, M., Wickham, J., Stehman, S., Auch, R., and Riitters, K.: Conterminous United States land cover change patterns 2001–2016 from the 2016 National Land Cover Database, ISPRS Journal of Photogrammetry and Remote Sensing, 162, 184-199, https://doi.org/10.1016/j.isprsjprs.2020.02.019, 2020.

Hong, C., Burney, J. A., Pongratz, J., Nabel, J., Mueller, N. D., Jackson, R. B., and Davis, S. J.: Global and regional drivers of land-use emissions in 1961-2017, Nature, 589, 554-561, https://doi.org/10.1038/s41586-020-03138-y, 2021.

Huang, C., Goward, S. N., Schleeweis, K., Thomas, N., Masek, J. G., and Zhu, Z.: Dynamics of national forests assessed using the Landsat record: Case studies in eastern United States, Remote Sensing of Environment, 113, 1430-1442, https://doi.org/10.1016/j.rse.2008.06.016, 2009.

Jin, H., Stehman, S. V., and Mountrakis, G.: Assessing the impact of training sample selection on accuracy of an urban classification: a case study in Denver, Colorado, International Journal of Remote Sensing, 35, 2067-2081, https://doi.org/10.1080/01431161.2014.885152, 2014.

Jin, S., Dewitz, J., Li, C., Sorenson, D., Zhu, Z., Shogib, M. R. I., Danielson, P., Granneman, B., Costello, C., Case, A., and Gass, L.: National Land Cover Database 2019: A Comprehensive Strategy for Creating the 1986–2019 Forest Disturbance Product, Journal of Remote Sensing, 3, https://doi.org/10.34133/remotesensing.0021, 2023.

795 Jin, S., Yang, L., Zhu, Z., and Homer, C.: A land cover change detection and classification protocol for updating Alaska NLCD 2001 to 2011, Remote Sensing of Environment, 195, 44-55, https://doi.org/10.1016/j.rse.2017.04.021, 2017.

Kennedy, R. E., Cohen, W. B., and Schroeder, T. A.: Trajectory-based change detection for automated characterization of forest disturbance dynamics, Remote Sensing of Environment, 110, 370-386, 800 https://doi.org/10.1016/j.rse.2007.03.010, 2007.

Kennedy, R. E., Yang, Z., and Cohen, W. B.: Detecting trends in forest disturbance and recovery using yearly Landsat time series: 1. LandTrendr — Temporal segmentation algorithms, Remote Sensing of Environment, 114, 2897-2910, https://doi.org/10.1016/j.rse.2010.07.008, 2010.

Li, X., Gong, P., and Liang, L.: A 30-year (1984–2013) record of annual urban dynamics of Beijing City derived 805 from Landsat data, Remote Sensing of Environment, 166, 78-90, https://doi.org/10.1016/j.rse.2015.06.007, 2015.

Liu, C., Zhang, Q., Luo, H., Qi, S., Tao, S., Xu, H., and Yao, Y.: An efficient approach to capture continuous impervious surface dynamics using spatial-temporal rules and dense Landsat time series stacks, Remote Sensing of Environment, 229, 114-132, https://doi.org/10.1016/j.rse.2019.04.025, 2019.

810 Liu, H., Gong, P., Wang, J., Wang, X., Ning, G., and Xu, B.: Production of global daily seamless data cubes and quantification of global land cover change from 1985 to 2020 - iMap World 1.0, Remote Sensing of Environment, 258, 112364, https://doi.org/10.1016/j.rse.2021.112364, 2021a.

Liu, L., Zhang, X., and Zhao, T.: GLC_FCS30D: the first global 30-m land-cover dynamic monitoring product with fine classification system from 1985 to 2022, Zenodo [data set], https://doi.org/ 10.5281/zenodo.8239305, 815 2023.

Liu, L., Zhang, X., Chen, X., Gao, Y., and Mi, J.: GLC_FCS30-2020:Global Land Cover with Fine Classification System at 30m in 2020 (v1.2), Zenodo [data set], https://doi.org/10.5281/zenodo.4280923 2020.

Liu, L., Zhang, X., Gao, Y., Chen, X., Shuai, X., and Mi, J.: Finer-Resolution Mapping of Global Land Cover: Recent Developments, Consistency Analysis, and Prospects, Journal of Remote Sensing, 2021, 5289697, 820 https://doi.org/10.34133/2021/5289697, 2021b.

Millard, K. and Richardson, M.: On the Importance of Training Data Sample Selection in Random Forest Image Classification: A Case Study in Peatland Ecosystem Mapping, Remote Sensing, 7, 8489-8515, https://doi.org/10.3390/rs70708489, 2015.

Pekel, J. F., Cottam, A., Gorelick, N., and Belward, A. S.: High-resolution mapping of global surface water and 825 its long-term changes, Nature, 540, 418-422, https://doi.org/10.1038/nature20584, 2016.

Pengra, B., Gallant, A., Zhu, Z., and Dahal, D.: Evaluation of the Initial Thematic Output from a Continuous Change-Detection Algorithm for Use in Automated Operational Land-Change Mapping by the U.S. Geological Survey, Remote Sensing, 8, 811, https://doi.org/10.3390/rs8100811, 2016.

Pontus Olofsson, G. M. F.: Good practices for estimating area and assessing accuracy of land change, Remote 830 Sensing of Environment, 148, 42-57, https://doi.org/10.1016/j.rse.2014.02.015, 2014.

Potapov, P., Hansen, M. C., Pickens, A., Hernandez-Serna, A., Tyukavina, A., Turubanova, S., Zalles, V., Li, X., Khan, A., Stolle, F., Harris, N., Song, X.-P., Baggett, A., Kommareddy, I., and Kommareddy, A.: The Global

2000-2020 Land Cover and Land Use Change Dataset Derived From the Landsat Archive: First Results, Frontiers in Remote Sensing, 3, https://doi.org/10.3389/frsen.2022.856903, 2022.

835 Potapov, P., Turubanova, S., Hansen, M. C., Tyukavina, A., Zalles, V., Khan, A., Song, X.-P., Pickens, A., Shen, Q., and Cortez, J.: Global maps of cropland extent and change show accelerated cropland expansion in the twenty-first century, Nature Food, 3, 19-28, https://doi.org/10.1038/s43016-021-00429-z, 2021.

Qin, Y., Xiao, X., Wigneron, J.-P., Ciais, P., Canadell, J. G., Brandt, M., Li, X., Fan, L., Wu, X., Tang, H., Dubayah, R., Doughty, R., Chang, Q., Crowell, S., Zheng, B., Neal, K., Celis, J. A., and Moore, B.: Annual
840 Maps of Forests in Australia from Analyses of Microwave and Optical Images with FAO Forest Definition, Journal of Remote Sensing, 2021, https://doi.org/10.34133/2021/9784657, 2021.

Radoux, J., Lamarche, C., Van Bogaert, E., Bontemps, S., Brockmann, C., and Defourny, P.: Automated Training Sample Extraction for Global Land Cover Mapping, Remote Sensing, 6, 3965-3987, https://doi.org/10.3390/rs6053965, 2014.

845 Roy, D. P., Kovalskyy, V., Zhang, H. K., Vermote, E. F., Yan, L., Kumar, S. S., and Egorov, A.: Characterization of Landsat-7 to Landsat-8 reflective wavelength and normalized difference vegetation index continuity, Remote Sensing of Environment, 185, 57-70, https://doi.org/10.1016/j.rse.2015.12.024, 2016.

Roy, D. P., Qin, Y., Kovalskyy, V., Vermote, E. F., Ju, J., Egorov, A., Hansen, M. C., Kommareddy, I., and Yan, L.: Conterminous United States demonstration and characterization of MODIS-based Landsat ETM+
850 atmospheric correction, Remote Sensing of Environment, 140, 433-449, https://doi.org/10.1016/j.rse.2013.09.012, 2014a.

Roy, D. P., Wulder, M. A., Loveland, T. R., C.E., W., Allen, R. G., Anderson, M. C., Helder, D., Irons, J. R., Johnson, D. M., Kennedy, R., Scambos, T. A., Schaaf, C. B., Schott, J. R., Sheng, Y., Vermote, E. F., Belward, A. S., Bindschadler, R., Cohen, W. B., Gao, F., Hipple, J. D., Hostert, P., Huntington, J., Justice, C. O., Kilic,
855 A., Kovalskyy, V., Lee, Z. P., Lymburner, L., Masek, J. G., McCorkel, J., Shuai, Y., Trezza, R., Vogelmann, J., Wynne, R. H., and Zhu, Z.: Landsat-8: Science and product vision for terrestrial global change research, Remote Sensing of Environment, 145, 154-172, https://doi.org/10.1016/j.rse.2014.02.001, 2014b.

Song, X. P., Hansen, M. C., Stehman, S. V., Potapov, P. V., Tyukavina, A., Vermote, E. F., and Townshend, J. R.: Global land change from 1982 to 2016, Nature, 560, 639-643, https://doi.org/10.1038/s41586-018-0411-9,
860 2018.

Stehman, S. V., Pengra, B. W., Horton, J. A., and Wellington, D. F.: Validation of the U.S. Geological Survey's Land Change Monitoring, Assessment and Projection (LCMAP) Collection 1.0 annual land cover products 1985–2017, Remote Sensing of Environment, 265, 112646, https://doi.org/10.1016/j.rse.2021.112646, 2021.

Sulla-Menashe, D., Gray, J. M., Abercrombie, S. P., and Friedl, M. A.: Hierarchical mapping of annual global
865 land cover 2001 to present: The MODIS Collection 6 Land Cover product, Remote Sensing of Environment, 222, 183-194, https://doi.org/10.1016/j.rse.2018.12.013, 2019.

Tachikawa, T., Hato, M., Kaku, M., and Iwasaki, A.: Characteristics of ASTER GDEM Version 2, Geoscience and Remote Sensing Symposium (IGARSS), 3657-3660, https://doi.org/10.1109/IGARSS.2011.6050017, 2011.

Venter, Z. S., Barton, D. N., Chakraborty, T., Simensen, T., and Singh, G.: Global 10 m Land Use Land Cover
870 Datasets: A Comparison of Dynamic World, World Cover and Esri Land Cover, Remote Sensing, 14, 4101, https://doi.org/10.3390/rs14164101, 2022.

Verbesselt, J., Hyndman, R., Newnham, G., and Culvenor, D.: Detecting trend and seasonal changes in satellite image time series, Remote sensing of Environment, 114, 106-115, https://doi.org/10.1016/j.rse.2009.08.014, 2010.

875   Vermote, E.: LEDAPS surface reflectance product description, available at: https://www.usgs.gov/media/files/landsat-4-7-collection-1-surface-reflectance-code-ledaps-product-guide (last access: 4 Augest 2023), 2007.

Vermote, E. F. and Kotchenova, S.: Atmospheric correction for the monitoring of land surfaces, Journal of Geophysical Research, 113, https://doi.org/10.1029/2007jd009662, 2008.

880   Wang, N., Zhang, X., Yao, S., Wu, J., and Xia, H.: How Good Are Global Layers for Mapping Rural Settlements? Evidence from China, Land, 11, 1308, https://doi.org/10.3390/land11081308, 2022.

Winkler, K., Fuchs, R., Rounsevell, M., and Herold, M.: Global land use changes are four times greater than previously estimated, Nat Commun, 12, 2501, https://doi.org/10.1038/s41467-021-22702-2, 2021.

Xian, G. Z., Smith, K., Wellington, D., Horton, J., Zhou, Q., Li, C., Auch, R., Brown, J. F., Zhu, Z., and Reker,

885   R. R.: Implementation of the CCDC algorithm to produce the LCMAP Collection 1.0 annual land surface change product, Earth Syst. Sci. Data, 14, 143-162, https://doi.org/10.5194/essd-14-143-2022, 2022.

Xie, S., Liu, L., Zhang, X., and Yang, J.: Mapping the annual dynamics of land cover in Beijing from 2001 to 2020 using Landsat dense time series stack, ISPRS Journal of Photogrammetry and Remote Sensing, 185, 201-218, https://doi.org/10.1016/j.isprsjprs.2022.01.014, 2022.

890   Yang, J. and Huang, X.: The 30 m annual land cover dataset and its dynamics in China from 1990 to 2019, Earth Syst. Sci. Data, 13, 3907-3925, https://doi.org/10.5194/essd-13-3907-2021, 2021.

Ye, S., Rogan, J., Zhu, Z., and Eastman, J. R.: A near-real-time approach for monitoring forest disturbance using Landsat time series: stochastic continuous change detection, Remote Sensing of Environment, 252, 112167, https://doi.org/10.1016/j.rse.2020.112167, 2021.

895   Zhang, H. K. and Roy, D. P.: Using the 500 m MODIS land cover product to derive a consistent continental scale 30 m Landsat land cover classification, Remote Sensing of Environment, 197, 15-34, https://doi.org/10.1016/j.rse.2017.05.024, 2017.

Zhang, X., Liu, L., Chen, X., Gao, Y., and Jiang, M.: Automatically Monitoring Impervious Surfaces Using Spectral Generalization and Time Series Landsat Imagery from 1985 to 2020 in the Yangtze River Delta, Journal

900   of Remote Sensing, 2021, 1-16, https://doi.org/10.34133/2021/9873816, 2021a.

Zhang, X., Liu, L., Chen, X., Gao, Y., Xie, S., and Mi, J.: GLC_FCS30: global land-cover product with fine classification system at 30 m using time-series Landsat imagery, Earth Syst. Sci. Data, 13, 2753-2776, https://doi.org/10.5194/essd-13-2753-2021, 2021b.

Zhang, X., Liu, L., Chen, X., Xie, S., and Gao, Y.: Fine Land-Cover Mapping in China Using Landsat Datacube

905   and an Operational SPECLib-Based Approach, Remote Sensing, 11, 1056, https://doi.org/10.3390/rs11091056, 2019.

Zhang, X., Liu, L., Wu, C., Chen, X., Gao, Y., Xie, S., and Zhang, B.: Development of a global 30 m impervious surface map using multisource and multitemporal remote sensing datasets with the Google Earth Engine platform, Earth Syst. Sci. Data, 12, 1625-1648, https://doi.org/10.5194/essd-12-1625-2020, 2020.

910   Zhang, X., Liu, L., Zhao, T., Chen, X., Lin, S., Wang, J., Mi, J., and Liu, W.: GWL_FCS30: a global 30 m wetland map with a fine classification system using multi-sourced and time-series remote sensing imagery in 2020, Earth Syst. Sci. Data, 15, 265-293, https://doi.org/10.5194/essd-15-265-2023, 2023.

Zhang, X., Liu, L., Zhao, T., Gao, Y., Chen, X., and Mi, J.: GISD30: global 30 m impervious-surface dynamic dataset from 1985 to 2020 using time-series Landsat imagery on the Google Earth Engine platform, Earth Syst.

915   Sci. Data, 14, 1831-1856, https://doi.org/10.5194/essd-14-1831-2022, 2022.

Zhang, Y., Ling, F., Wang, X., Foody, G. M., Boyd, D. S., Li, X., Du, Y., and Atkinson, P. M.: Tracking small-scale tropical forest disturbances: Fusing the Landsat and Sentinel-2 data record, Remote Sensing of Environment, 261, 112470, https://doi.org/10.1016/j.rse.2021.112470, 2021c.

920 Zhao, T., Zhang, X., Gao, Y., Mi, J., Liu, W., Wang, J., Jiang, M., and Liu, L.: Assessing the Accuracy and Consistency of Six Fine-Resolution Global Land Cover Products Using a Novel Stratified Random Sampling Validation Dataset, Remote Sensing, 15, 2285, https://doi.org/10.3390/rs15092285, 2023.

Zhu, Z.: Change detection using landsat time series: A review of frequencies, preprocessing, algorithms, and applications, ISPRS Journal of Photogrammetry and Remote Sensing, 130, 370-384, https://doi.org/10.1016/j.isprsjprs.2017.06.013, 2017.

925 Zhu, Z., Gallant, A. L., Woodcock, C. E., Pengra, B., Olofsson, P., Loveland, T. R., Jin, S., Dahal, D., Yang, L., and Auch, R. F.: Optimizing selection of training and auxiliary data for operational land cover classification for the LCMAP initiative, ISPRS Journal of Photogrammetry and Remote Sensing, 122, 206-221, https://doi.org/10.1016/j.isprsjprs.2016.11.004, 2016.

Zhu, Z., Wang, S. X., and Woodcock, C. E.: Improvement and expansion of the Fmask algorithm: cloud, cloud

930 shadow, and snow detection for Landsats 4-7, 8, and Sentinel 2 images, Remote Sensing of Environment, 159, 269-277, https://doi.org/10.1016/j.rse.2014.12.014, 2015.

Zhu, Z. and Woodcock, C. E.: Automated cloud, cloud shadow, and snow detection in multitemporal Landsat data: An algorithm designed specifically for monitoring land cover change, Remote Sensing of Environment, 152, 217-234, https://doi.org/10.1016/j.rse.2014.06.012, 2014a.

935 Zhu, Z. and Woodcock, C. E.: Continuous change detection and classification of land cover using all available Landsat data, Remote Sensing of Environment, 144, 152-171, https://doi.org/10.1016/j.rse.2014.01.011, 2014b.

Zhu, Z., Woodcock, C. E., and Olofsson, P.: Continuous monitoring of forest disturbance using all available Landsat imagery, Remote Sensing of Environment, 122, 75-91, https://doi.org/10.1016/j.rse.2011.10.030, 2012.

Zhu, Z., Zhang, J., Yang, Z., Aljaddani, A. H., Cohen, W. B., Qiu, S., and Zhou, C.: Continuous monitoring of

940 land disturbance based on Landsat time series, Remote Sensing of Environment, https://doi.org/10.1016/j.rse.2019.03.009, 2019.